Uncertainty quantification of the ONERA 7A rotor using comprehensive analysis

Manas Khurana, Itham Salah El Din, Hyeonsoo Yeo

Uncertainty Quantification of the ONERA 7A Rotor Performance and Loads Using Comprehensive Analysis

Manas Khurana*
Science and Technology Corporation, Moffett Field, California 94035
Itham Salah El din†
ONERA—The French Aerospace Lab, Meudon 92190, France
and
Hyeonsoo Yeo‡
U.S. Army Combat Capabilities Development Command, Moffett Field, California 94035

Quantification of blade stiffness uncertainties and sensitivities on rotor power and structural loads for the ONERA 7A rotor is established using the U.S. Army and ONERA rotorcraft comprehensive analysis tools. A stochastic-based approach is implemented to generate probabilistic bounds of the response outputs, including rotor performance and loads due to uncertainties in blade stiffness using 1) a Monte Carlo approach coupled directly with U.S. Army's rotorcraft comprehensive toolset, and 2) a surrogate of ONERA's rotorcraft comprehensive analysis solver using polynomial chaos expansions to efficiently predict the response outputs. The analysis showed that uncertainties in blade torsion, flap, and lag stiffnesses impact the predicted rotor power by a quantifiable amount. Significant uncertainties in peak torsion, flap, and chord bending moments are also confirmed. The sensitivities of the stiffness properties on response outputs using Sobol indices are also studied. The results show that total required power is exclusively sensitive to variability in torsion stiffness with no interaction effects with flap and lag stiffnesses. Sensitivities due to independent parameter effects and by combining with other parameters on peak structural loads are also examined. The analysis demonstrates the merits of integrating a stochastic, data-driven approach for uncertainty and sensitivity analyses in rotorcraft aeromechanics predictions.

Nomenclature

CBM	=	chord bending moment, N · m
C_L	=	rotor lift coefficient
C_T	=	rotor thrust coefficient
$\mathrm{EI}_{\mathrm{flap}}$	=	normalized flap stiffness
$\mathrm{EI}_{\mathrm{lag}}$	=	normalized lag stiffness
FBM	=	flap bending moment, N · m
GJ	=	normalized torsion stiffness
N	=	number of uncertain variables
$\mathcal{N}(\mu, \sigma)$	=	normal distribution (mean, standard deviation)
P	=	rotor power, HP
TM	=	torsion moment, N · m
$Z_{\alpha/2}\frac{\sigma}{\sqrt{n}}$	=	standard-of-error
μ	=	mean
ρ_N	=	normal probability density function
σ	=	blade solidity or standard deviation
σ_μ	=	standard error of the mean
Ψ_j	=	polynomial chaos expansion basis
Ω	=	probability design space

I. Introduction

ADVANCED modeling and simulation tools are needed in rotorcraft design for predictive performance analysis. Aerodynamic performances and loads, in general, cannot be accurately predicted using deterministic solvers, and safety factors are typically used as fail-safe mechanisms to design robust and certified flight systems. Computational methods regardless of fidelity have parameter and model form uncertainties that propagate through the engineering analysis, resulting in variability in response outputs. Accordingly, the outputs will likely differ from expected performances because of the unaccounted uncertainty in the model.

There have been rapid advancements in computational power that have resulted in the development of advanced rotorcraft tools, including the state-of-the-art HPCMP CREATE-AV Helios [1] and elsA [2]. The capabilities of these methods can be further enhanced by incorporating the impact of system uncertainties, both epistemic and aleatory on model responses. The impact of aleatory uncertainties on the accurate estimation of helicopter performance and loads has not been studied in detail. It has been discussed in the literature that stochastic model inputs can significantly influence the design process where the achievement of system performance goals cannot be guaranteed due to the inherent uncertainties in the inputs [3]. The goal of this task is to account for uncertainties for rotorcraft applications so that an accurate representation of the performance envelope can be established using statistical metrics. To address this need, the methodologies presented in this work support the transition from deterministic to a stochastic-based analysis.

Comprehensive analysis (CA) tool chains are widely used for rotorcraft performance and loads assessment, and these methods will be used in the present study to address the research outcomes. The CA tools that will be applied in the calculation of rotor power and blade structural loads include the Rotorcraft Comprehensive Analysis System (RCAS) [4] and the Helicopter Overall Simulation Tool (HOST) [5]. RCAS, developed by the U.S. Army, is a comprehensive multidisciplinary, computer software system. HOST, developed by Airbus Helicopters, is also a rotorcraft CA tool that models blade dynamics using a multibody scheme [6]. The solvers are used to first establish code-to-code comparison of input–output on a common problem-of-interest and are then used to verify the influence of the dependencies in uncertainty propagation. This will involve the identification and characterization of the system uncertainties and sensitivities on quantity-of-interest (QoI) by using the outputs of the deterministic method. Access to this critical information will facilitate capabilities in model knowledge, including risk management and mitigation. The study will ultimately define the role of uncertainty quantification (UQ) in computational rotorcraft aeromechanics so that methodology benefits when integrated

*Research Aerospace Engineer, Ames Research Center. Member AIAA.

† Research Aerospace Engineer, Department of Aerodynamics, Aeroelasticity and Acoustics.

‡ Research Aerospace Engineer, Aviation and Missile Center, Ames Research Center. Associate Fellow AIAA.

into the available CA tool chain set and eventually into higher-fidelity codes are identifiable. The data established will permit the definition of flight performance and load variance envelopes with probability intervals, and this knowledge will guide informed decision making as part of the aircraft design cycle.

Application of UQ methods for aerospace applications has been documented in the literature [7–9]. In support of a stochastic-based analysis, Lee et al. [10] documented guidelines for the verification and validation (V&V) of computing simulations that incorporate error and uncertainty sources during the modeling, verification, and validation processes, with the goal of estimating the total prediction uncertainty of a simulation. The practices proposed have been used as a baseline for follow-up works in the field. Baurle and Axdahl [7] used computational fluid dynamics (CFD) to model both aleatory and epistemic uncertainties in a highly backpressured scramjet isolator flowfield. The analysis confirmed that discretization error has a significant influence on system uncertainties. Beran et al. [8] modeled aircraft aeroelastic interactions, and proposed a mixed-fidelity approach with CFD to efficiently drive the UQ process. Stanford and Massey [9] also used CFD to model the influence of the parametric uncertainties, including atmospheric flow and structural variables of a generic transport wing model configuration on the damping character of the dynamic aeroelastic wing response due to some perturbation.

Quantification of system uncertainties for rotorcraft applications using CA tools has also been documented in the literature. Singh et al. [11] used RCAS to model the performance uncertainties of a new Hover Validation and Acoustic Baseline (HVAB) rotor blade with prescribed distribution (uncertainty) in blade structural properties. The analysis confirmed that the magnitude of the difference between the established statistical mean of the output response, C_T/σ, due to input torsion stiffness uncertainty was less than 1% in comparison to the deterministic (without uncertainty) value. Anusonti-Inthra et al. [12] performed sensitivity and uncertainty analysis of a coaxial corotating rotor system in hover using RCAS. They showed that pitch control settings and performance metrics are sensitive to variability in the center-of-gravity placement of the platform. It was also shown that the hub forces and moments are sensitive to changes in ambient drift speeds where stochastic-based derived data due to input uncertainty are different compared to deterministic derived data when uncertainty is not factored in the analysis. Murugan et al. [13] modeled the effects of spatially uncertain material properties on the aeroelastic response predictions (rotating blade natural frequencies and vibratory hub loads) of a composite helicopter rotor. In the analysis, it was shown that spatial uncertainty has considerable impact on aeroelastic response predictions where uncertainty in composite properties significantly influences the rotating frequencies of the rotor blades. It was also shown that the uncertainty effects on the rotating frequencies vary with higher frequency flap, lag, and torsion modes. Sensitivity analysis (SA) also showed that frequencies of flap, lag, and torsion are influenced by the uncertainties in stiffness at the root and inboard sections of the rotor blade. In additional works by Siva et al. [3], the effects of structural and aerodynamic uncertainties on the performance predictions of an untwisted and linearly twisted rotor blade were investigated using Monte Carlo simulation (MCS). The analysis confirmed uncertainties in rotor power in hover and axial climb phases. In comparison to baseline performance without uncertainties, the magnitude of differences between stochastic mean and baseline result was more than 25% for rotor power. The largest uncertainty in power coefficient was established for a forward flight case, hence enforcing the need to carefully select an appropriate powerplant that will attain the desired performance requirements. The UQ and SA methodologies presented in this work further support these research efforts by performing code-to-code comparisons with RCAS and HOST on the ONERA 7A rotor at high speed. Further, a comparative analysis using different uncertainty propagation methods with MCS (U.S. Army) and a surrogate-assisted simulation approach (ONERA) are evaluated to assess data convergence.

The contributions of this work add to the current body-of-knowledge related to uncertainty analysis for rotorcraft aeromechanics. Here, the impact of uncertainties in blade stiffness on rotor power and blade structural loads is established. The work documented in the literature [11,12] addresses simplified hover cases, yet in this work the UQ analysis is extended to high-speed forward-flight scenarios. Further, the parameterization of stiffness uncertainties is also induced using uniform and nonuniform methods to compare the effect of input stiffness mapping schemes on uncertainty in rotor performance and loads.

The paper is organized as follows: Sec. II outlines the scope of the study, which includes the introduction of the 7A rotor reference test case, including the validation of the numerical solver used to establish rotor performance and loads, followed by a preliminary parametric analysis for cross-validation purposes; Sec. III introduces fundamental uncertainty analysis concepts and the propagation of aleatory uncertainties through the proposed UQ framework; in Sec. IV, UQ and global sensitivity analyses are undertaken; and in Sec. V, main conclusions are summarized.

II. Study Scope

The uncertainties in blade properties on rotor performance and structural loads are investigated. In this section, an overview of the study scope is summarized:

1) CA tools and test model: RCAS and HOST solvers are introduced, including the ONERA 7A rotor blade.

2) Dynamic inflow model is established to validate number of states using RCAS and HOST with available test data.

3) Parametric analysis is performed to establish the relationships between blade stiffness (inputs to the UQ study) on loads and rotor performance.

4) Uncertainty quantification includes the following:

a) Concept theory and background

b) Uncertainty propagation using MCS and a surrogate-based polynomial chaos expansion (PCE) approach

5) SA using PCE is introduced.

A. Rotorcraft Comprehensive Analysis and Test Model

RCAS, developed by the U.S. Army, is a comprehensive, multidisciplinary, computer software system for predicting rotorcraft aerodynamics, performance, stability and control, aeroelastic stability, loads, and vibration. RCAS can model a wide range of complex rotorcraft configurations operating in hover, forward flight, and maneuvering conditions. The RCAS structural model employs a hierarchical, finite element, multibody dynamics formulation for coupled rotor–body systems. HOST used by ONERA is also a rotorcraft CA tool that was developed by Airbus Helicopters. HOST modeling of blade dynamics is based on a multibody approach. The blade is represented as an assembly of rigid segments connected by virtual joints. Euler-beam modeling provides three degrees of freedom, namely, flapwise bending, chordwise bending, and torsion. RCAS and HOST have similar aerodynamic models. The aerodynamics is based on a lifting-line approach with airfoil lookup tables combined with a wake model. In this effort, among the several wake models available, finite-state dynamic inflow model is used in both analyses.

The ONERA 7A rotor blade operating at a high-speed condition ($\mu = 0.40, C_L/\sigma = 0.063$) is used as a test model. The configuration was extensively tested in the ONERA S1MA transonic wind tunnel for rotor performance and loads data and was previously investigated using various analysis tools and methods [6,14–16]. The 7A rotor is a four-bladed fully articulated rotor, with a radius of 2.1 m and solidity σ of 0.084. The blade shown in Fig. 1 is of rectangular planform and uses two airfoils, the OA213 and OA209. Figure 1 also shows the locations of structural loads measurements from strain gauges. Flap bending moments (FBMs) are available at six radial locations (30, 40, 55, 65, 75, and 85%R). However, chord bending moments (CBMs) are available at three radial locations (30, 40, and 85%R) and torsion moments (TMs) are available at five radial locations (30, 40, 55, 65, and 75%R). During the test, the rotor was trimmed to satisfy the Modane flapping law ($\beta_{1s} = 0, \beta_{1c} = -\theta_{1s}$) in addition to the specified rotor lift and propulsive force using rotor collective and cyclic controls and shaft angle.

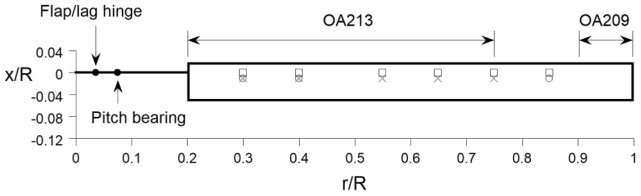

Fig. 1 The 7A blade plan form with structural loads measurements (□: flap bending; ∘: chord bending; ×: torsion moment measurements).

In RCAS, the blade was analyzed using 16 nonlinear beam elements and 22 aerodynamic segments shown in Fig. 2. Similar discretization was also implemented in HOST with 25 spanwise elements used for the computational analysis. Both analyses modeled the rotor hub as fully articulated with pitch bearing and flap and lag hinges. The elastomeric lag damper of the 7A rotor was modeled with equivalent hinge stiffness and damping values at the lag hinge. A 5.0° (72 steps per rotor revolution) azimuthal step size was used for trim in RCAS, and a 6.0° azimuthal step size was used in HOST.

In Ref. [15], blade natural frequencies were calculated as a function of rotor speed using RCAS and HOST. The predictions by the two comprehensive codes showed excellent agreement with each other for low-frequency modes. This confirms that the structural dynamics models of the two analyses are equivalent.

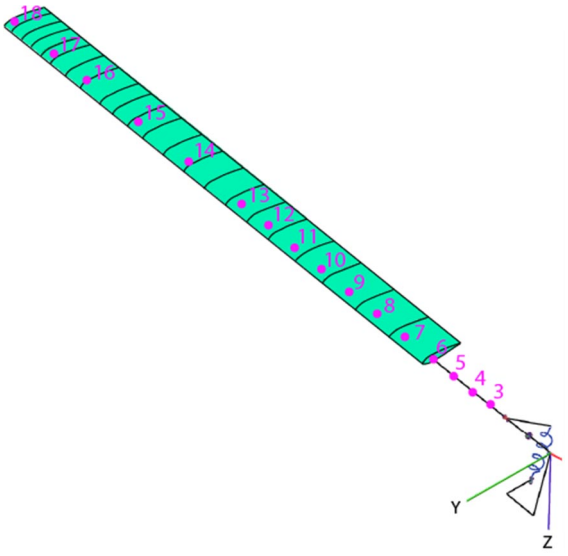

Fig. 2 The 7A rotor blade modeling using comprehensive analysis (shown here is the RCAS configuration).

B. Inflow Model Validation with Experiment

A validated inflow model is to be established as a baseline for the uncertainty analysis to follow. In this setup, the goal was to establish an acceptable balance between computational efficiency and solver accuracy using the proposed CA tools. The present study used the finite-state dynamic inflow model, which was based on the actuator disk solution of the three-dimensional potential flow equations. The induced velocity is expressed in terms of Fourier harmonics (for azimuthal variations) and Legendre functions (for radial variations). In an *m*-by-*n* dynamic inflow model, *m* represents the number of harmonics and *n* represents the highest power in the Legendre polynomials. In the analysis, half peak-to-peak blade structural loads are established as a function of the number of inflow states. Figure 3 compares the RCAS predictions for TM, FBM, and CBM results with the measured data along the blade span.

The analysis in Fig. 3 confirmed that, as the number of inflow states is increased, the calculated peak-to-peak structural loads decrease and converge to the experimental data. Although not shown, the analysis showed the same convergence trends for rotor power. The computational disparity between an 8×8 and 12×12 state model is negligible, yet the computational effort in the two cases was noticeable. Accordingly, an 8×8 model was selected as the baseline for follow up UQ works due to an acceptable balance between computational agreement with experiment and computing resources needed for a converged solution.

A dynamic inflow study was also performed with HOST, and similar trends from Fig. 3 were noted for the convergence of rotor power and bending moment loads. Direct comparison of RCAS and HOST data with experiment is presented in Fig. 4. The analysis confirms acceptable convergence of RCAS and HOST data for TMs and FBMs with experiment, yet both analyses overpredict the CBM. Yeo et al. [15] has shown that the RCAS calculations coupled with Helios CFD code reduced the half peak-to-peak CBMs and significantly improved the correlation, but the HOST calculations coupled with elsA CFD code overpredicted the CBMs. The reasons for the observed differences are not known.

C. Parametric Analysis

As outlined at start of Sec. II, parametric analysis is undertaken to map the trends between uncertain inputs on response outputs. A scaling factor (SF) is introduced, which acts as a multiplier to the baseline stiffness to induce systematic and uniform variations to flap (EI_{flap}), lag (EI_{lag}), and torsion (GJ) stiffness across a range of 40–200%. In this case, each parameter is varied one at a time, while other properties are fixed at their baseline setting. At each increment change, the rotor power and structural loads, including TMs, FBMs and CBMs, are calculated. Figure 5 represents the test envelope of the variations in EI_{flap} and GJ that were induced in RCAS relative to the baseline setting.

As a result of the induced parametric variations, the impact on rotor power using RCAS is presented in Fig. 6. The analysis

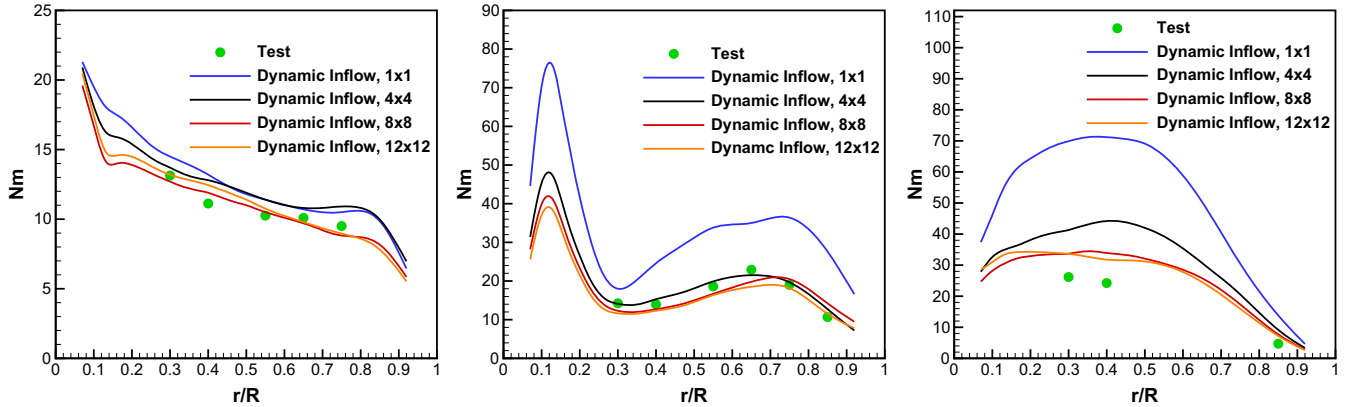

a) Torsion moment [Nm] **b) Flap bending moment [Nm]** **c) Chord bending moment [Nm]**

Fig. 3 Half peak-to-peak structural loads: convergence of dynamic inflow model with test data using RCAS.

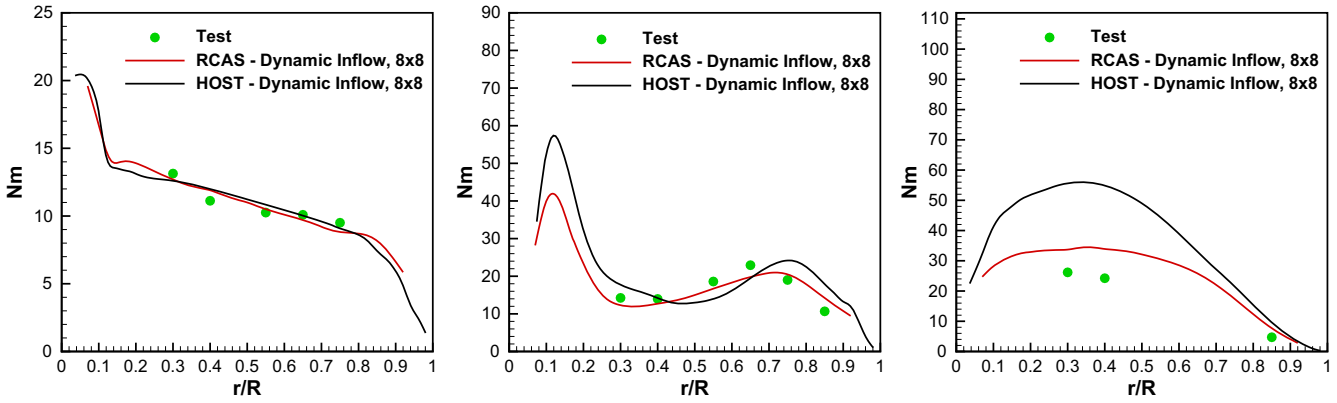

a) Torsion moment [Nm] b) Flap bending moment [Nm] c) Chord bending moment [Nm]

Fig. 4 Analysis of structural loads using RCAS and HOST with test data.

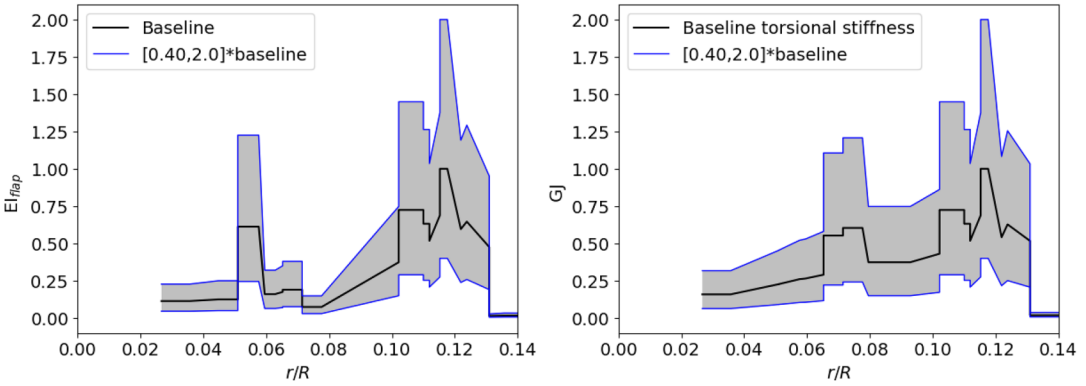

a) Flap stiffness: EI_{flap} b) Torsion stiffness: GJ

Fig. 5 RCAS: test envelope (shaded region) for design parametric analysis relative to baseline (solid line); stiffness values are normalized by the corresponding maximum values.

confirmed that power is sensitive to changes in GJ, and relatively power remains unchanged due to the variability in lag and flap stiffness. Critically it is noted that there is a penalty in rotor power as GJ decreases. In the earlier analysis by Jain and Yeo [17], this pattern was also established with the UH-60A rotor in high-speed forward flight. This was attributed to the distribution of the average drag across the rotor disk, which was observed to increase as GJ was decreased such that there was a higher drag penalty on the outboard region of the retreating side. Accordingly, an increase in rotor power follows to maintain trimmed flight.

Comparison of rotor power with variability in torsion stiffness using RCAS and HOST is presented in Fig. 7. The general trends are

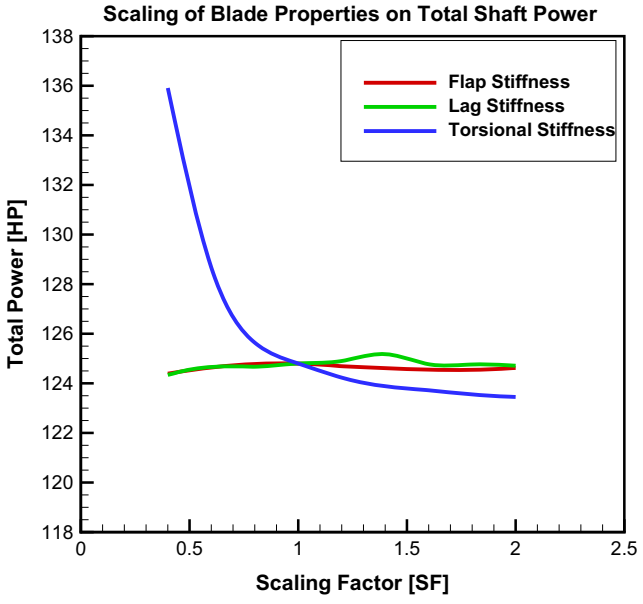

Fig. 6 RCAS: impact of blade stiffness variation on rotor power.

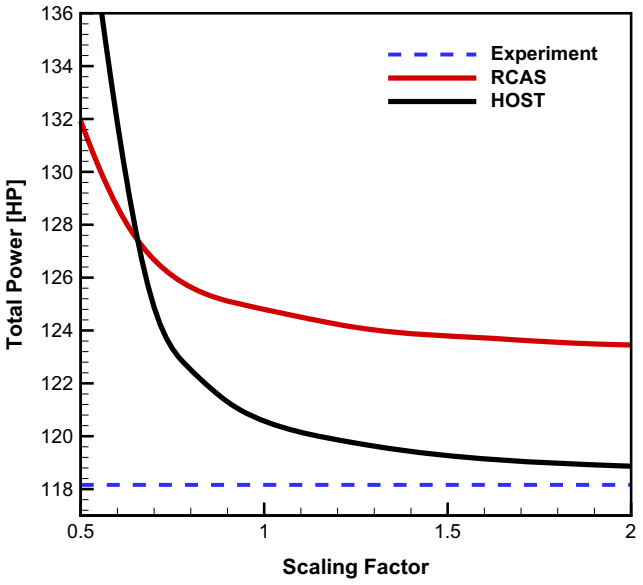

Fig. 7 Rotor power due to scaling of GJ established using RCAS and HOST.

captured by both analyses. At nominal stiffness with SF = 1.0, high-speed experimental power equals 118.16 HP [6], and at this setting RCAS predicted 124.80 HP. In comparison, HOST yields closer agreement relative to RCAS at 120.57 HP, yet this reading is also overpredicted relative to experiment. Despite the disparity between the two results, the data trends confirm that a valid analysis can follow for the quantification of 7A rotor blade performance and loads uncertainties due to stiffness variability.

As next step, a scatter plot with 500 Latin hypercube sampling (LHS) points is generated to assess the trends between blade stiffness properties on rotor power and peak loads in Fig. 8. A r- correlation coefficient is calculated to quantify the trends between inputs and outputs and is bounded between values of -1 and 1 to assess the strength of the linear relationship between the parameters. Values near 1 indicate strong positive correlation; -1 represents strong negative correlation; and 0 represents no correlation. Critically the analysis only factors the linearities between the parameters and does not confirm the degree of nonlinearity.

The linear regression scatter plot in Fig. 8 shows the following:

a) GJ has moderate linear relationship with rotor power and peak FBM and CBM, yet nonlinearity with peak TM is observed.

b) Variation in flap stiffness exhibits strong linear trend with peak FBM and moderate negative correlation with peak TM, yet against rotor power and peak CBM, nonlinear patterns are noted. Also confirmed is the overall magnitude of change in rotor power (y axis between 124.4 and 124.8 HP) and peak TM (y axis between 18 and 20 N · m) is minimal, hence indicating that the respective outputs are insensitive to flap stiffness.

c) Sampling of lag stiffness only exhibits notable linear trend with rotor power although the overall change in performance is minimal (y axis between 124.5 and 125 HP). Nonlinear trends are confirmed for all peak loads where peak TM is observed to be insensitive (y axis between 18 and 20 N · m) to variation in lag stiffness. The results confirm that parametric-based approaches can be used to assess input sensitivity on uncertain outputs if the dimensionality is low. If the uncertain input space becomes large, the parameters are likely to exhibit complex nonlinear trends due to the coupling effects by the different combinations of the input parameters, and these relationships cannot be quantified using systematic parametric-based approaches.

As next step, the variation in GJ and $\mathrm{EI}_{\mathrm{flap}}$ on spanwise TMs and FBMs with RCAS and HOST is presented. As a general trend in both analyses, it is observed that as GJ increases in Fig. 9, the TM across the span decreases slightly. This pattern (GJ on peak TM) was also confirmed in the sensitivity matrix plot in Fig. 8, where an r-correlation of -0.63 was established. In general, changes in torsion stiffness have a small influence on TM except when there is a significant reduction in GJ as noted when the SF $= 0.40$. Figure 10 shows fan plot of the 7A blade. Solid lines represent the blade frequencies with the baseline properties and dotted lines represent those with 40 and 200% of baseline GJ values, respectively. Note that $\mathrm{EI}_{\mathrm{flap}}$ and $\mathrm{EI}_{\mathrm{lag}}$ values are the same as baseline values for the frequency calculation. Torsion stiffness has a substantial influence on the blade torsion frequencies (about 4.1/rev with 40%GJ and about 8.4/rev with 200%GJ). Due to pitch–flap coupling, flap frequencies also changed slightly. The baseline torsion frequency is about 6.3/rev. As torsional stiffness is reduced, torsion frequency also decreases. Initially there is a small change in the peak-to-peak TM amplitude. However, as the torsion frequency approaches 4/rev, the peak-to-peak loads starts to increase. Although the absolute values are different (Fig. 9), similar pattern is captured in both RCAS and HOST analyses except for the lowest stiffness value. HOST analysis shows significantly higher TM for the 50% of baseline GJ value case. The reasons for this discrepancy are not known.

The impact of flap stiffness on spanwise FBM is further presented in Fig. 11. Flap stiffness has a significant influence on spanwise FBM (also confirmed in matrix sensitivity plot in Fig. 8). As expected, the spanwise FBM increases, including the maximum peak-to-peak load at $r/R \approx 0.125$, as $\mathrm{EI}_{\mathrm{flap}}$ increases and the spanwise FBM decreases as $\mathrm{EI}_{\mathrm{flap}}$ decreases. Both RCAS and HOST show a similar trend.

The parametric analysis shown in Figs. 6–9 and 11 confirms that performance variability in power and structural loads exists due to changes in blade stiffness. Both RCAS and HOST data exhibit matching performance trends despite the disparity in solver accuracy relative to experiment. It has also been established in Fig. 8 that nonlinear trends are present in the design space; hence a sampling study using a stochastic-based approach is warranted for the quantification of response output uncertainties due to variability in blade stiffness.

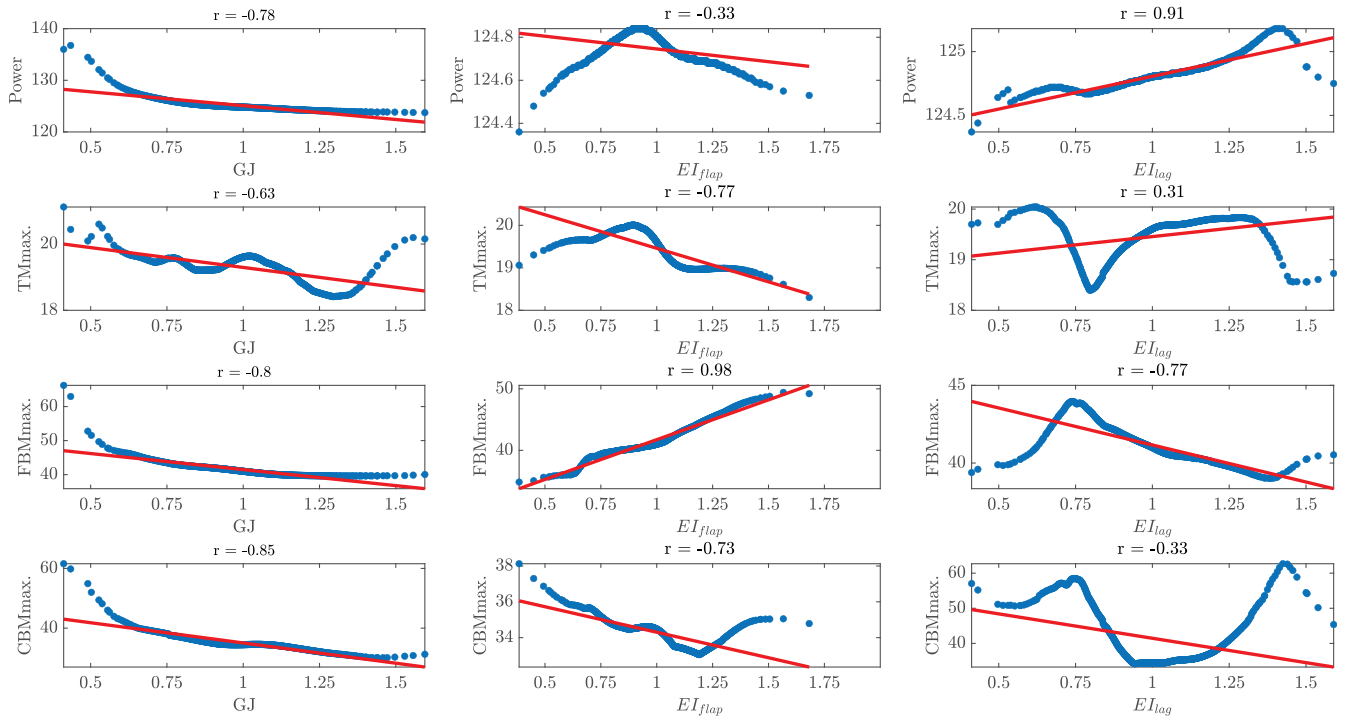

Fig. 8 Latin hypercube sampling of 500 points representing the relationship between blade stiffness parameters on rotor power and peak loads using RCAS.

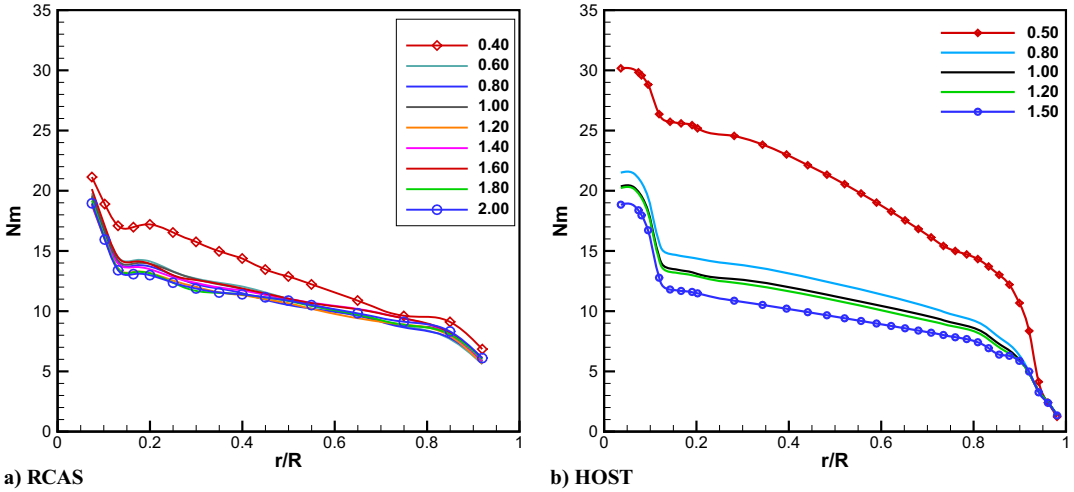

a) RCAS b) HOST

Fig. 9 Spanwise distribution of torsion moment due to variability in GJ spanning 40–200% relative to baseline.

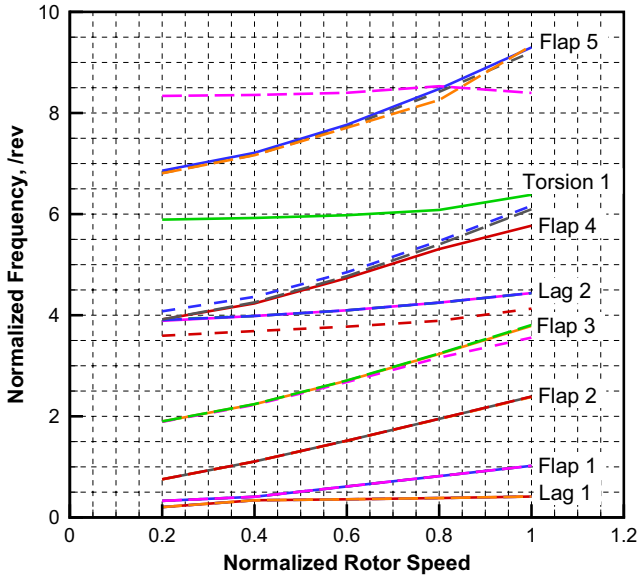

Fig. 10 Blade frequency with GJ variation.

III. Uncertainty Quantification and Sensitivity Analysis

In this section, a brief overview of the UQ and SA approaches will be presented. The uncertainty framework will include a description of the probabilistic method in the form of 1) the Monte Carlo–based approach and 2) the computationally efficient PCE method. SA will provide an overview of the global variability approach using the Sobol indices (SIs). The computational implementation of these methods will then follow including an overview of the statistical measures that support data postprocessing from the response outputs.

A. Uncertainty Quantification

The model f is considered as a black box and represents the underlying system (in this case, the CA tools, RCAS, and HOST), which is analyzed by solving the governing equations. Here f is the general model with output Y such that $Y = f(\boldsymbol{x})$, where $\boldsymbol{x} = [x_1, x_2, \ldots, x_k]^T$ is a vector of k inputs to the model with associated probability distributions.

$$Y = f(\boldsymbol{x}) \tag{1}$$

The output Y is any value in the output space Ω with an unknown probability density function (PDF), ρ_Y, that is established using a uncertainty propagation scheme. This involves the determination of the distribution of Y for function f in Eq. (1) based on the distributions of the input parameters of $\boldsymbol{x}_k$. The uncertain input parameters are characterized using a normal (Gaussian) distribution with mean μ and standard deviation σ such that $N(\mu, \sigma)$. The PDF of the normal distribution $\rho_N(\boldsymbol{x})$ is denoted by

$$\rho_N(\boldsymbol{x}) = \frac{1}{\sigma\sqrt{2\pi}} e^{-\frac{1}{2}\left(\frac{x-\mu}{\sigma}\right)^2} \tag{2}$$

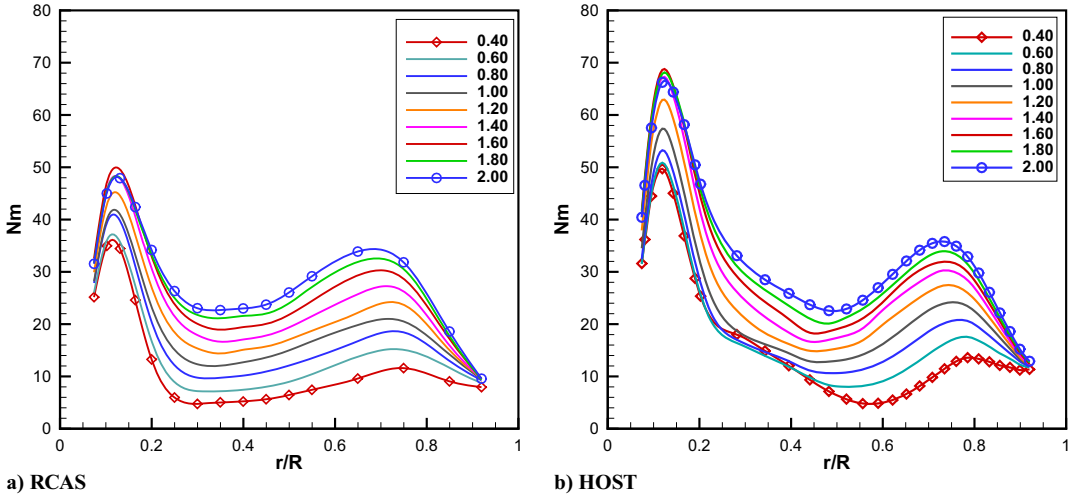

a) RCAS b) HOST

Fig. 11 Spanwise distribution of flap bending moment due to variability in EI_{flap} spanning 40–200% relative to baseline.

Once the input parameters $\boldsymbol{x}$ are propagated into the model, f (CA or surrogate), the uncertainty metrics of a continuous random variable X are established from the statistics of the PDF, ρ. This can include the mean $\mathbb{E}$ (expectation value) and variance $\mathbb{V}$. The mean is defined as

$$\mathbb{E}[X] = \int_{\Omega} \boldsymbol{x} \cdot \rho(\boldsymbol{x})\, \mathrm{d}\boldsymbol{x} \tag{3}$$

The statistical measures are calculated using moment i, with Eq. (4) representing the variance ($i = 2$):

$$\mathbb{V}[X] = \int_{\Omega} (\boldsymbol{x} - \mathbb{E}[X])^{i=2} \cdot \rho(\boldsymbol{x})\, \mathrm{d}\boldsymbol{x} \tag{4}$$

where the ith moment represents the variance ($i = 2$), skewness ($i = 3$), and kurtosis ($i = 4$).

Postprocessing of UQ data is carried out by generating a cumulative distribution function (CDF) that is representative of the area under the PDF. It is used to evaluate the probability P that output Y will take a value less than or equal to a set threshold y such that

$$f_Y(y) = P(Y \leq y) \tag{5}$$

The probability that Y is in the interval $(a, b]$ such that $a < b$ is denoted by

$$P(a < Y \leq b) = f_y(b) - f_y(a) \tag{6}$$

The CDF permits the assessment of critical design questions, for example: *Given the uncertainties in blade properties, what is the probability that rotor load will exceed a critical safety threshold?*

B. Uncertainty Propagation Analysis Method

1. Monte Carlo Approach

A widely used probabilistic approach for uncertainty propagation is the Monte Carlo method. The framework can facilitate UQ in a nonintrusive manner as it does not require the modification of the underlying solver, and it also does not make any assumptions about the model. The method randomly selects the input parameters from the input PDFs across the ranges of uncertain variables, $\boldsymbol{x}$, of size N by a stratified sampling scheme. The model is then evaluated at sample $\boldsymbol{x}$ that creates the mapping of the inputs to outputs:

$$[\boldsymbol{x_i}, y_i], \quad i = 1, 2, \ldots, N$$

where $y_i = f(\boldsymbol{x_i})$. Equations (3) and (4) are used to calculate the statistics of the response output, and the process is repeated by increasing sampling size N until statistical convergence of the outputs is achieved. The mapping of inputs to outputs can be postprocessed using scatterplots to assess the relationships (linear, nonlinear, discontinuities), or a least-squares approach is used to form a regression model that relates output to inputs. Additional statistical analysis is also undertaken to generate output PDFs and CDFs, leading to the quantification of response intervals with probabilities due to input uncertainties.

Uncertainty propagation with MCS will converge to the exact stochastic solution as the sample population, $N \to \infty$. Yet, the convergence of the mean error, σ_μ, estimate will be limited as the standard deviation of the mean scales inversely with the square root of the sample size:

$$\sigma_\mu = \frac{\sigma}{\sqrt{N}} \tag{7}$$

Consequently statistical convergence is assessed using a) mean in Eq. (3); b and c) convergence of PDF and CDF curves; and d) standard error based on the 97.5th percentile point of a standard distribution $Z_{\alpha/2}$ (in this case $Z_{\alpha/2} = 1.96$), allowing to establish the 95% probability confidence interval (CI) as follows:

$$CI = \left[\mu - Z_{\alpha/2}\frac{\sigma}{\sqrt{N}}, \mu + Z_{\alpha/2}\frac{\sigma}{\sqrt{N}}\right] \tag{8}$$

When $N \to \infty$, the confidence interval length will be zero and reduced to the real statistical mean. Hence, a significant limitation of the MC approach is that it requires many function evaluations for statistical convergence.

One approach to limit this issue involves improving the coverage of the parameter space for the distribution of the input samples. Accordingly LHS developed by McKay et al. [18] is used for uncertainty propagation. In this approach, the range of each input random variable is divided into intervals with equal probability. The methodology has been extensively used in a wide range of applications [19–23], including rotorcraft conceptual design [24] and uncertainty analysis with NASA rotorcraft sizing design tools [25]. Even with improved stratified sampling for uncertainty propagation, the MC approach with direct model evaluations is a computationally expensive process especially if high-fidelity simulations govern the solver. To adequately address this issue, a metamodel is needed for the system response.

2. Polynomial Chaos Expansion Surrogate Modeling

Surrogate modeling is implemented to replace the computationally expensive deterministic model for uncertainty propagation. The goal is to formulate a methodology that will accurately approximate the system response using a limited set of data over a defined space. Surrogate modeling is beneficial in scenarios where many calls to the computational model are required, for design optimization, and in this case for uncertainty propagation. The development of a surrogate model requires a finite number of deterministic simulations to form a regression model by fitting the system response as a function of the design space.

In this work, the nonintrusive polynomial chaos (NIPC) method is used. The approach has been applied for a wide range of aerospace applications by Schaefer et al. [20], Debusschere et al. [26], Najm [27], and Hosder et al. [28]. In this process, the NIPC is developed by iteratively increasing the number of deterministic evaluations until a surrogate model with desired accuracy and convergence is established. Here the NIPC method is briefly defined, and a thorough summary of the model is available in the literature [29]. If we consider, again, the uncertain (random) variable x and its realization y, if the latter has a finite variance, it can be represented as a second-order random process using a PCE:

$$y = \sum_{j=1}^{\infty} a_j \Psi_j(x) \tag{9}$$

The a_j coefficients can be considered as the coordinates of y in the space generated from the polynomial chaos basis, Ψ_j. Consider a single random variable problem for sake of clarity before a generalized formulation is provided. The first step is to define the polynomial basis expression. For every analytic probability distribution of a random variable, an orthogonal polynomial basis can be defined. Commonly used distributions and the associated polynomial chaos basis are defined in Table 1.

The polynomial chaos functions of a given family are mutually orthogonal, according to the following inner product in a Hilbert space, Ω, for x:

Table 1 Polynomial chaos families correspondence with standardized distribution laws

Variable distribution law	Polynomial chaos	Support
Uniform	Legendre	$[a, b]$
Gaussian (normal)	Hermite	$(-\infty, +\infty)$
Gamma	Laguerre	$[0, \infty]$
Beta	Jacobi	$[a, b]$

$$\langle \Psi_k(x); \Psi_l(x) \rangle = \int_\Omega \Psi_k(x)\Psi_l(x)\rho(x)\,\mathrm{d}x = \langle \Psi_k(x)^2 \rangle \delta_{kl} \tag{10}$$

where δ_{kl} is the Kronecker delta function and ρ is the PDF. The summation in Eq. (9) must be truncated to establish the desired maximum polynomial degree. The truncation limit p depends on the polynomial *degree* d (maximum value) and the random vector dimension n (= 1 for single variable problem), providing an expression of the approximation of the random response, $\tilde{y}$, according to the polynomial chaos coefficients $\tilde{a}_j$:

$$\tilde{y}(x) = \sum_{j=0}^{p} \tilde{a}_j \Psi_j(x) \quad \text{with } p+1 = \frac{(d+n)!}{d!n!} \tag{11}$$

The truncation scheme introduces an error that is measured by expressing $y(x) - \tilde{y}(x)$ as

$$y(x) - \tilde{y}(x) = \sum_{j=0}^{p} (a_j - \tilde{a}_j)\Psi_j(x) + \sum_{j=p+1}^{\infty} a_j \Psi_j(x) \tag{12}$$

The norm of the error is obtained using the inner product and the orthogonality properties of the polynomial basis:

$$\|y(x) - \tilde{y}(x)\|^2 = \sum_{j=0}^{p} (a_j - \tilde{a}_j)^2 \|\Psi_j\|^2 + \sum_{j=p+1}^{\infty} a_j^2 \|\Psi_j\|^2 \tag{13}$$

The error is minimal when the estimation error is equal to zero; i.e. $(a_j = \tilde{a}_j)\ \forall\ j \in \{0, 1, \ldots, p\}$, leaving only the truncation error. Once the truncation is defined, the coefficients a_j are calculated using the orthogonality properties of the PCE basis:

$$a_j(x) = \frac{\langle y(x); \Psi_j(x) \rangle}{\langle \Psi_j(x)^2 \rangle} \tag{14}$$

knowing that

$$\langle y(x); \Psi_j(x) \rangle = \int_\Omega y(x)\Psi_j(x)\rho(x)\,\mathrm{d}x$$

There are two methods to establish the coefficients a_j. The first is to compute the integral using a Gaussian quadrature. The integral can be approximated using a polynomial expansion γ_i on a discrete number of evaluations of the random vector $(x_1, \ldots, x_q)$. This vector includes collocation points corresponding to the chosen polynomials zeros location in the exploration space. The integral can then be approximated as follows:

$$\int_\Omega y(x)\Psi_j(x)\rho(x)\,\mathrm{d}x \tilde{=} \sum_{i=0}^{q} y(x_i)\Psi_j(x_i)\omega_i \tag{15}$$

The weighting factor ω_i is obtained using the Gauss quadrature method. The benefit of this approach is that it can accurately interpolate between the input sampling dataset as long as the function evaluations are executed at the prescribed quadrature points. Additional details of this methodology are provided in [30].

In the second technique for the calculation of a_j, the quadratic error between the model and approximated value is minimized [31]. In this case, the evaluations are not restrained to quadrature locations, but the accuracy of the regression is guided by both the input sampling as well as the minimization algorithm efficiency.

As extension to multivariate problems, a multi-index vector is introduced:

$$I = \left\{ \alpha \in \mathbb{N}^d, |\alpha| = \sum_{i=0}^{d} \alpha_i \le d \right\}$$

And a polynomial chaos $\Psi^i_{\alpha_i}$ of order α_i is associated with random variable x_i, where the PCE assumption that the random variables are independent is defined as follows:

$$\rho = \prod_{i=1}^{n} \rho_i(x_i) \tag{16}$$

Equation (11) can then be extended:

$$\tilde{y}(x) = \sum_{\alpha \in I} a_\alpha \Psi_\alpha(x) \quad \text{with } \Psi_\alpha(x) = \prod_{i=1}^{n} \Psi^i_{\alpha_i}(x_i) \tag{17}$$

The a_α coefficients are obtained using the expression transposed from Eq. (14). In this study, the regression approach is used to mitigate solver nonconvergence issues at the quadrature point locations.

3. *Sensitivity Analysis Using Polynomial Chaos Expansion*

Variance-based decomposition methods such as analysis of variance (ANOVA) for linear approaches or global sensitivity analysis (GSA) for nonlinear functions provide an insight on the weight of the variable randomness on output response. The GSA proposed by Sobol [32,33] uses SIs that quantify the fractional effect of each random variable, including higher-order interactions effect on model output. It is shown that there is a unique decomposition of y that is integrable on Ω with respect to each random variable using the ANOVA representation:

$$y(x) = y_0 + \sum_{i=1}^{n} y_i(x_i) + \sum_{i=1}^{n}\sum_{j=1}^{n} y_{i,j}(x_i, x_j) + \sum \ldots + y_{1,\ldots,n}(x_1, \ldots, x_n) \tag{18}$$

provided that

$$\int_\Omega y_{k_1,\ldots,k_s}(x_{k_1}, \ldots x_{k_s})\,\mathrm{d}x_{k_m} = 0 \quad \forall\ (k_1, k_s)/\{1 \le k_1 < \ldots < k_s \le n\} \quad \forall\ s \in [1, n]$$

In the first term in Eq. (18), y_0 is constant and represents the mean of the model, y. The total variance is expressed as

$$\mathbb{V}(y) = \int_\Omega y^2(x)\,\mathrm{d}x - y_0^2 \tag{19}$$

and for each function of the decomposition,

$$\mathbb{V}_{k_1,\ldots,k_s} = \int_\Omega \cdots \int_\Omega y^2_{k_1,\ldots,k_s}(x)\,\mathrm{d}x_{k_1} \ldots \mathrm{d}x_{k_s} \quad \forall\ (k_1, k_s)/\{1 \le k_1 < \ldots < k_s \le n\} \quad \forall\ s \in [1, n] \tag{20}$$

The first order and second order, including total SIs, are generated from the variance as follows:

$$S_i = \frac{\mathbb{V}(\mathbb{E}[y|x_i])}{\mathbb{V}(y)} = \frac{\mathbb{V}_i}{\mathbb{V}(y)} \tag{21}$$

$$S_{i,j} = \frac{\mathbb{V}_{i,j}}{\mathbb{V}(y)} \tag{22}$$

$$S_{Ti} = S_i + \sum_{j=1}^{n} S_{i,j} + \sum_{j=1}^{n}\sum_{k=1}^{n} S_{i,j,k} + \ldots \tag{23}$$

The SIs further have the following property:

$$\sum_{k_1,k_s} S_{k_1,\ldots,k_s} = 1 \quad \forall\ (k_1,k_s)/\{1 \le k_1 < \ldots < k_s \le n\}$$
$$\forall\ s \in [1,n] \tag{24}$$

The indices can be evaluated using the Monte Carlo approach, but Sudret [34] showed that the PCE approach can also be used to efficiently generate the SI values. As both the PCE and the SI approaches provide a similar decomposition, and considering the PCE basis orthogonality properties, the SI first-order can be expressed using the PCE coefficients:

$$S_i = \frac{\sum_{\alpha \in I_i} a_\alpha^2}{\sum_{\alpha \in I^*} a_\alpha^2} \quad \text{with}$$
$$\begin{cases} I_i = \{\alpha \in I, \alpha_i \neq 0,\ \forall\ j \neq i \alpha_j = 0\} \\ I^* = \left\{\alpha = (\alpha_1,\ldots,\alpha_i,\ldots,\alpha_m) \in \mathbb{N}^m, \sum_{i=1}^m \alpha_i \le d \text{ and } \alpha \neq 0^m\right\} \end{cases} \tag{25}$$

For the second order, the SI is

$$S_{i,j} = \frac{\sum_{\alpha \in I_{i,j}} a_\alpha^2}{\sum_{\alpha \in I^*} a_\alpha^2}$$
$$\text{with } I_{i,j} = \{\alpha \in I; \alpha_i, \alpha_j \neq 0;\ \forall\ k \neq ietk \neq j \alpha_k = 0\} \tag{26}$$

And for the total SI,

$$S_{Ti} = 1 - \frac{\sum_{\alpha \in \tilde{I}_i} a_\alpha^2}{\sum_{\alpha \in I^*} a_\alpha^2} \quad \text{with } \tilde{I}_i = \{\alpha \in I, \alpha_i = 0,\ \forall\ j \neq i \alpha_j \neq 0\} \tag{27}$$

The analysis assumes that the uncertain input variables are statistically independent, else the application of the Rosenblatt [35] transformation would be warranted.

IV. Numerical Analysis

In this section, uncertainty and sensitivity of the ONERA 7A rotor blade are established. The analysis will address the following questions:

1) *Uncertainty analysis:* How do the uncertainties in blade stiffness properties impact rotor power and half peak-to-peak (HPP) structural loads?

2) *Sensitivity analysis:* Which blade stiffness property has the greatest contribution to overall uncertainty in rotor power and structural loads, and where in the blade (radial span stations)?

As first step, the identification of the sources of uncertainties in blade properties is required. A UQ-based computational framework is then exercised using a propagation scheme with MCS and a surrogate-assisted model. A SA approach using a global nonlinear method with SIs then follows to identify blade properties and regions that are most influential on total system variability.

A. System Uncertainties

The classification of uncertain blade stiffness properties are defined in Table 2. Variability in blade stiffness properties is characterized to be aleatory uncertain due to the inherent randomness in spanwise blade properties as a result of manufacturing variations which are introduced due to imprecise equipment, varied raw material properties, and heat treatment processes. At predefined blade regions, an SF is applied, as a multiplier to the baseline setting to impose stiffness variability for the uncertainty analysis. In the absence of real-life manufacturing data that can be referenced indicating design fabrication tolerances and/or defects during assembly leading to variances in blade properties, the scope-of-randomness for aleatory parameter definition is assumed in this work. Here the SF is set to be normally distributed with mean, $\mu = 1.0$ (blade at baseline state). At initial analysis, two standard deviations were tested at $\sigma = 10\%$ and $\sigma = 20\%$ (variability of uncertainty about the nominal state). In the preliminary analysis, it was established that at $\sigma = 10\%$, the uncertainties in rotor power and maximum peak-to-peak loads were negligible. Accordingly in the analysis to follow, the standard deviation was increased to $\sigma = 20\%$ for both RCAS and HOST studies to then establish if at a higher variability, performance uncertainties will follow.

Table 2 RCAS study: representation of uncertain stiffness input parameters to establish impact on rotor power and structural loads (torsion, flap, and chord bending moments)

Stiffness	Parameter (SF)	PDF	Mean (μ)	Std. dev. (σ)
GJ	SF_{GJ}	Normal	1.0	0.20
EI_{flap}	$SF_{EI_{flap}}$	Normal	1.0	0.20
EI_{lag}	$SF_{EI_{lag}}$	Normal	1.0	0.20

The parameterization of blade stiffness was *uniformly* induced using a constant SF at each radial station spanning from root to tip. The impact of these uncertainties has been studied using two different approaches. Firstly, the uncertainty of the maximum half peak-to-peak loads along the span is considered, and, secondly, the comparison of the variability at the blade span locations where the blade structural loads were measured with strain gauges is considered. The first study is performed using the MC strategy coupled directly to CA, while the alternate approach takes advantage of a CA surrogate-based approach.

B. Uncertainty Analysis Using Monte Carlo Simulations

The uncertainty in blade stiffness properties on response outputs is quantified using RCAS with 1500 LHS generated Monte Carlo runs. Ideally the simulation sample size needs to be governed by a statistically converged result, but to maintain reasonable computing overheads, the maximum run size was capped. The sample size adopted will provide an acceptable design space coverage (although not fully converged) from which expected data trends can be established for the assessment of system uncertainties.

1. *Blade Stiffness Versus Rotor Power*

Initially each stiffness parameter is sampled using LHS one-at-a-time before the combined effects of all three stiffness parameters (GJ, EI_{flap}, EI_{lag}) are integrated to study the coupling effects. The results in Tables 3–6 represent the response output for rotor power and maximum spanwise half peak-to-peak loads. In each table, the dashed line (- - - - -) characterizes deterministic RCAS response when the stiffness is at baseline (SF = 1.0; nominal stiffness setting without uncertainties); the bullet symbol (•) represents mean from the Monte Carlo runs; the 95% probability distribution from the MC runs is captured by establishing the 2.5th and the 97.5th percentile of the distribution from the CDF to then form the 95% probability width (|——|) of the responses. Accordingly the uncertainties in blade stiffness properties on rotor power are summarized in Table 3.

Uncertainty in GJ on rotor power is summarized in the top row of Table 3. The variability in rotor power using the 95% probability interval width (difference between 2.5 and 97.5% cumulative probability bounds) is much bigger than the other cases modeled. An interval width of 4.13 HP is ≈3.00% of the deterministic value of 124.81 HP, where no uncertainties are factored. The sensitivity of rotor power to GJ is expected from the parametric analysis in Figs. 6 and 8, where a decrease in rotor power with increasing torsion stiffness was established.

In the postprocessing analysis to follow, the PDF of the response outputs is established using the MATLAB Statistics and Machine Learning Toolbox [36]. In Fig. 12b, it is established that rotor power follows an asymmetric generalized extreme value (GEV) probability distribution [36,37] with extreme outliers in the tails of the curve. The GEV distribution represents a family of continuous probability distributions that are based on the extreme value theory (EVT) [38]. EVT provides the statistical framework to make inferences about the probability of extreme outlier events in the distributed sample set. From the power PDF, the MCS statistical mean of 125.10 HP was

Table 3 Representation of normally distributed, $\mathcal{N}(1.0, 0.20)$, blade stiffness uncertainties on rotor power (P_{req}) using 95% probability intervals

Uncertain stiffness	P_{req} (Det. = 124.81 HP)	μ	2.5% Prob.	97.5% Prob.	Width
GJ		125.10	123.90	128.03	4.13
EI_{flap}		124.75	124.39	124.84	0.45
EI_{lag}		124.81	124.58	125.02	0.44
GJ, EI_{flap}, EI_{lag}		125.03	123.91	127.85	3.94
	123 124 125 126 127 128				

Table 4 Representation of normally distributed, $\mathcal{N}(1.0, 0.20)$, blade stiffness uncertainties on maximum torsion moment (TM_{max}) using 95% probability intervals

Uncertain stiffness	TM_{max}. (Det. = 19.60 N · m)	μ	2.5% Prob.	97.5% Prob.	Width
GJ		19.30	18.52	20.22	1.70
EI_{flap}		19.46	18.00	20.00	2.00
EI_{lag}		19.46	18.48	20.00	1.52
GJ, EI_{flap}, EI_{lag}		19.16	18.31	20.40	2.09
	18 18.5 19 19.5 20 20.5				

Table 5 Representation of normally distributed, $\mathcal{N}(1.0, 0.20)$, blade stiffness uncertainties on maximum flap bending moment (FBM_{max}) using 95% probability intervals

Uncertain stiffness	FBM_{max}. (Det. = 41.00 N)	μ	2.5% Prob.	97.5% Prob.	Width
GJ		41.49	39.54	51.70	12.16
EI_{flap}		41.74	36.52	47.21	10.69
EI_{lag}		41.16	39.23	44.07	4.84
GJ, EI_{flap}, EI_{lag}		42.23	36.60	51.37	14.77
	40 45 50				

Table 6 Representation of normally distributed, $\mathcal{N}(1.0, 0.20)$, blade stiffness uncertainties on maximum chord bending moment (CBM_{max}) using 95% probability intervals

Uncertain stiffness	CBM_{max}. (Det. = 34.50 N · m)	μ	2.5% Prob.	97.5% Prob.	Width
GJ		35.04	30.60	42.14	11.54
EI_{flap}		34.30	33.11	35.85	2.74
EI_{lag}		41.46	34.30	58.42	24.12
GJ, EI_{flap}, EI_{lag}		42.50	32.00	65.40	33.4
	35 40 45 50 55 60 65				

established, which is greater than the deterministic result of $P_{det.} = 124.81$ HP. The data confirm that skewness in rotor power with extreme outliers follows due to input uncertainty using the normal distribution where the stochastic mean is higher than baseline when no uncertainties are factored.

The CDF in Fig. 12c is generated to assess the probability intervals due to GJ uncertainty. A symmetric 95% probability interval between 2.5 and 97.5% cumulative probability bounds is generated (shaded in Fig. 12c) to assess the performance intervals in power performance. Critically, off-design performance with probability can also be established using the CDF. Assuming a critical power of 129.00 HP, the probability that rotor power due to GJ uncertainty will be less than this setting is ≈99%.

In Table 3, the variability in rotor power due to independent modeling of the uncertainty in EI_{flap} and EI_{lag} is also presented. Propagation of uncertainty in EI_{flap} resulted in a Monte Carlo–established mean of $P_{req} = 124.75$ HP, which was slightly lower than baseline, and the propagation of uncertainty in EI_{lag} resulted in Monte Carlo mean power that equaled the baseline result. The 95% probability interval bands for both EI_{flap} and EI_{lag} cases were also relatively narrow in comparison to the GJ case. In the parametric analysis in Fig. 6 and SA in Fig. 8, it was shown that the variability in EI_{flap} and EI_{lag} had a minimal impact on rotor power. A decrease in rotor power was obtained as EI_{flap} and EI_{lag} are independently lowered about the baseline at SF = 1.0. Accordingly, the data

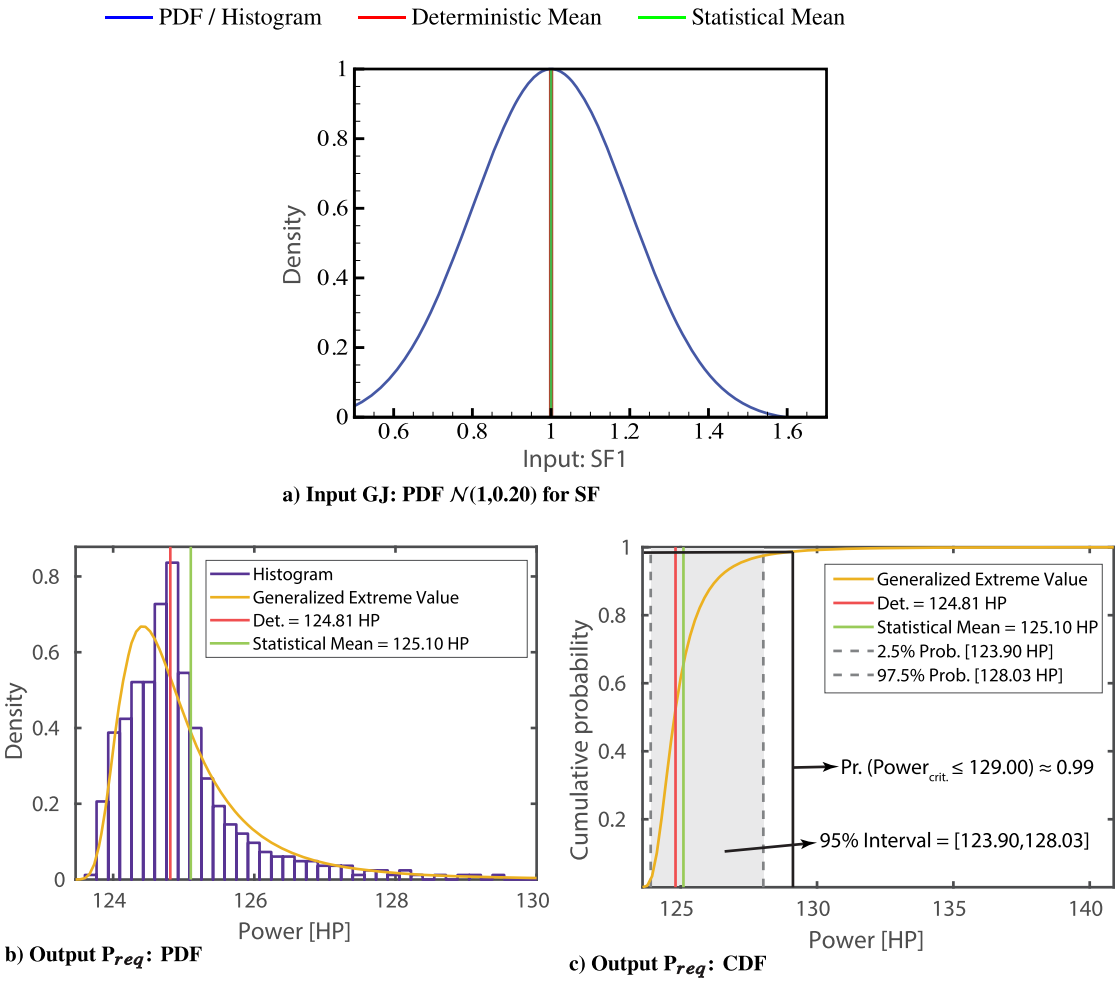

a) Input GJ: PDF $\mathcal{N}(1,0.20)$ for SF

b) Output P_{req}: PDF

c) Output P_{req}: CDF

Fig. 12 Uncertainty propagation of GJ on P_{req}.

sampled in the MCS using the prescribed distribution, $\mathcal{N}(1.0, 0.20)$, further re-enforced this pattern.

The data in Table 3 further present the combined effects of uncertainties in GJ, EI_{flap}, and EI_{lag} on rotor power. The Monte Carlo–established mean is only slightly greater than the baseline result, and the width of the 95% probability intervals matches the earlier GJ result such that it is ≈3.00% of the deterministic value. The results confirm that GJ alone has an active influence on rotor power in comparison to uncertainties in EI_{flap} and EI_{lag}. Hence, from a design perspective, uncertainty in GJ for the 7A rotor blade needs to be managed to ensure that vehicle power requirements are not violated.

2. *Blade Stiffness Versus Maximum Torsion Moment*

The uncertainties in blade stiffness parameters on maximum TM is presented in Table 4. The mean with variability in GJ results with TM_{max} equaling 19.30 N · m, which is lower than the nominal deterministic result (no uncertainties factored) at 19.60 N · m. In the supporting analysis (not presented here), it was noted that as GJ increases, the torsion frequency also increases, and for the 7A rotor, the peak-to-peak TM decreases relative to the baseline where the stiffness SF equals ones. This pattern was also confirmed in the parametric analysis in Fig. 9a, where an increase in GJ resulted in a decrease in TM_{max}. To represent system uncertainties, the 95% probability interval width was generated at 1.70 N · m, which is ≈9% of the deterministic result.

Uncertainties in EI_{flap} and EI_{lag} yield matching Monte Carlo result where TM_{max} mean at 19.46 N · m is lower than baseline at 19.60 N · m for both stiffness parameters. Yet, the 95% probability interval width representing the range of performance values expected due to respective EI uncertainties is ≈10% relative to the deterministic value for EI_{flap} compared to ≈8% for EI_{lag}.

Due to the combined stiffness effects, the mean Monte Carlo result at 19.16 N · m is further lower than baseline at 19.60 N · m. This is expected as each individual stiffness contribution independently resulted in the lowering of the Monte Carlo mean than deterministic, and these effects are further projected in the combined stiffness study. To further analyze the propagation of input uncertainty on TM_{max}, the data from the stochastic analysis are presented using a PDF and CDF in Fig. 13.

The PDF in Fig. 13a is formed using the maximum likelihood estimation (MLE) method to determine the parameters of a probability distribution that fit the sampled TM data by maximizing a likelihood function. Based on the fitting analysis, the PDF follows the GEV distribution. Accordingly, the EVT is applied to make inferences of extreme deviations in maximum TM due to the stochastic patterns of the sampled dataset. This is interpreted through a CDF in Fig. 13b, where a probability of ≈98% is established that TM maximum will be less than an assumed critical threshold of $TM_{max} = 20.50$ N · m. The CDF further provides a symmetric 95% probability range of 18.31–20.40 N · m due to input uncertainties centered around the data median (Table 4 and shaded in Fig. 13b). These data can then be used for ongoing design refinements if point estimate probabilities for a given load condition are not within acceptable thresholds.

3. *Blade Stiffness Versus Maximum Flap Bending Moment*

Uncertainties in blade stiffness parameters on maximum FBM are presented in Table 5. Independent uncertainty in GJ, EI_{flap}, and EI_{lag} results in a converged Monte Carlo mean that is marginally higher than the deterministic result. Importantly the uncertainty bands are quantified using the 95% probability interval where uncertainty in GJ leads to expected FBM_{max} loads spanning 39.54 N · m through 51.70 N · m with an overall width that is approximately 30% relative to the deterministic result of

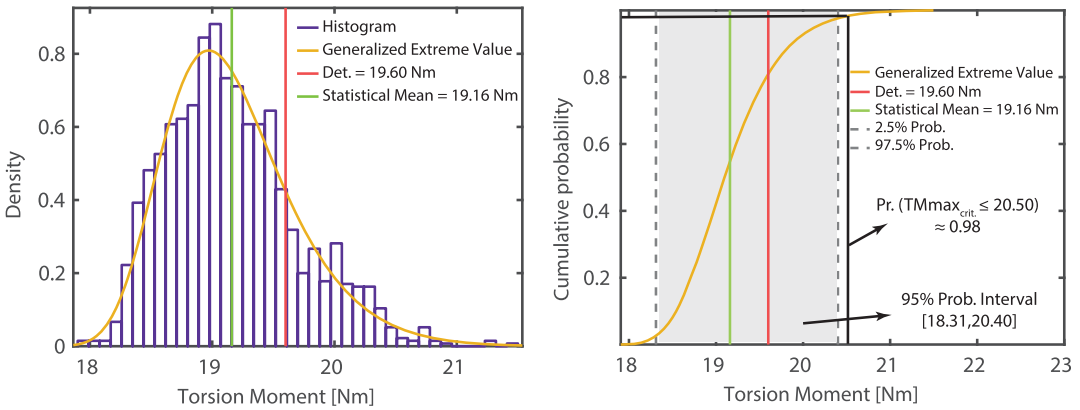

a) PDF **b) CDF**

Fig. 13 Statistical representation of the uncertainties in GJ, EI_{flap}, and EI_{lag} on maximum TM.

41.00 N · m. The uncertainty bands are also asymmetrical about the deterministic and Monte Carlo mean result. A similar trend is also established for uncertainty in EI_{flap} where the 95% probability interval is ≈26% relative to the deterministic measure and the uncertainty bands are symmetrical about the baseline (no uncertainties factored) and Monte Carlo mean measure. Further, uncertainty in EI_{lag} also constitutes to a symmetrical distribution of the 95% probability intervals about the Monte Carlo mean and matching deterministic result, yet the width of the uncertainty bands is reduced to ≈12% relative to uncertainties interval width for GJ and EI_{flap} conditions alone. This result infers that lag stiffness has a reduced effect with sensitivity on $FBM_{max.}$ than variability in GJ and EI_{flap} (confirmed in Fig. 8 also).

In the combined effects with uncertainties in GJ, EI_{flap}, and EI_{lag}, the mean $FBM_{max.}$ from the Monte Carlo run equals 42.23 N · m, which is about the baseline result at 41.00 N · m and matches closely to the means from the uncertainties of the individual blade stiffness parameters. Yet, the width of the uncertainty band is extended relative to previous cases analyzed at ≈36% relative to the deterministic result. Further probabilistic analysis with the corresponding uncertainties is analyzed in Fig. 14.

The PDF in Fig. 14a follows the GEV distribution where the fitting was estimated using the MLE method. The GEV distribution mean is 42.23 N · m (——) which is higher than the deterministic performance at 41.00 N · m (——), where blade stiffness is at the nominal setting. The analysis confirms that $FBM_{max.}$ expectation value formed using a stochastic framework with uncertainties is greater than the $FBM_{max.}$ load established using a deterministic framework where input uncertainties are not factored. The PDF further shows that at the tail there are extreme cases where $FBM_{max.}$ exceeds 60.00 N · m. The probabilities of the established design loads are interpreted using a CDF in Fig. 14b. The probability that blade $FBM_{max.}$ will be below the deterministic threshold such that $FBM_{max.} \leq 41.00$ N · m (—— in Fig. 14b) is ≈42%; the probability that a blade will be characterized with extreme $FBM_{max.} > 53.00$ N · m (—— in Fig. 14b) is ≈1%; and the 95% probability intervals are formed by establishing the interval width between 2.5 and 97.5% cumulative probability bounds resulting in intervals of 36.60–51.37 N · m (Table 5 and shaded in Fig. 14b between - - - - lines).

4. *Blade Stiffness Versus Maximum Chord Bending Moment*

The impact of uncertainties in blade stiffness parameters on maximum CBM is presented in Table 6. The Monte Carlo–established mean with independent modeling of uncertainty in GJ and EI_{flap} resulted in an expectation value that was close the deterministic result. The 95% probability interval with uncertainty in GJ resulted in a performance width that spanned ≈33% of the baseline result. Yet, uncertainty in EI_{flap} resulted in a $CBM_{max.}$ performance band that was ≈8% of the deterministic result. Hence, it is concluded that uncertainty in EI_{flap} will have negligible impact on $CBM_{max.}$.

With uncertainty in EI_{lag}, the mean $CBM_{max.}$ from the Monte Carlo runs and the 95% probability bands increase relative to the GJ and EI_{flap} cases. In the parametric analysis that was performed (not shown here), it was observed that EI_{lag} is at an optimum (minimal) state when stiffness scaling is at a nominal (baseline) setting. A subtle deviation (increase or decrease) in stiffness about the deterministic threshold results in a significant increase in $CBM_{max.}$ loads. These trends are further shown in Table 6, where variability in EI_{lag} using a normal distribution of the SF (Table 2) results in a Monte Carlo mean and 95% probability performance bands that are higher than the baseline condition and the cases analyzed with uncertainties GJ and EI_{flap} conditions. Further, the width of the $CBM_{max.}$ performance band is ≈70% of the deterministic result, hence confirming that a wide range of $CBM_{max.}$ loads are expected due to uncertainty in EI_{lag}.

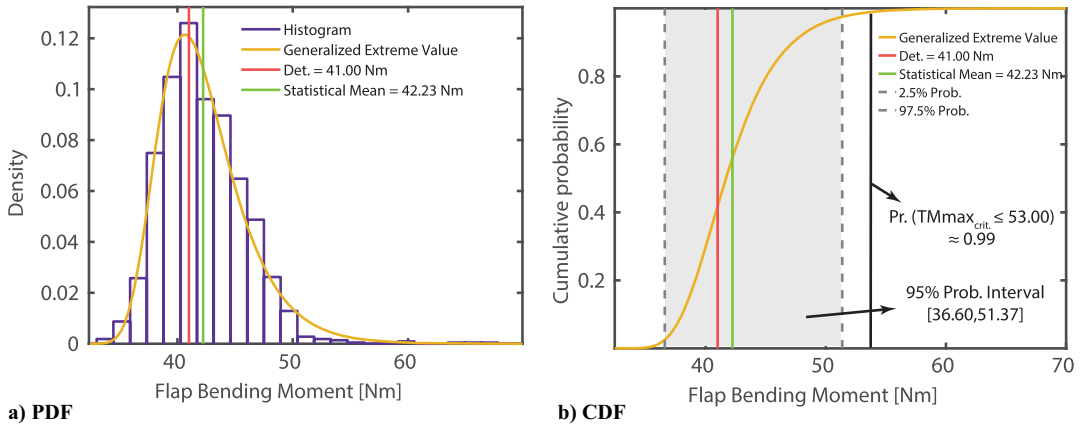

a) PDF **b) CDF**

Fig. 14 Statistical representation of the uncertainties in GJ, EI_{flap}, and EI_{lag} on maximum FBM.

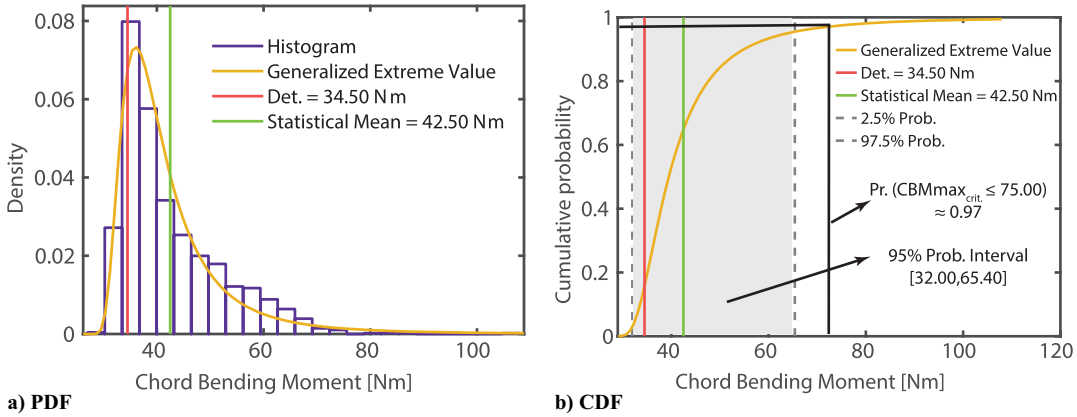

a) PDF **b) CDF**

Fig. 15 Statistical representation of the uncertainties in GJ, EI_{flap}, and EI_{lag} on maximum CBM.

Due to the combined uncertainties of the three stiffness parameters, the Monte Carlo mean and the 95% probability intervals width increase relative to the other cases analyzed. In the absence of a formal sensitivity study, the systematic analysis presented (Table 6) confirms that the active parameter causing the extended width of the $CBM_{max.}$ performance band is due to the uncertainty in EI_{lag} followed by GJ with EIflap causing minimal influence. The performance width established is significant and extends to ≈97% of the baseline result, which confirms that uncertainties in stiffness parameters, specifically in EI_{lag}, need to be mitigated to reduce the performance output domain.

Further analysis is undertaken by the representation of the output data distribution and corresponding probabilities using a PDF and CDF, respectively, in Fig. 15. The output PDF in Fig. 15a follows the GEV distribution that is positively skewed and was established using the MLE approach. Due to the input uncertainties, discrepancy between the baseline result (34.50 N · m, ——) and Monte Carlo mean at 42.50 N · m (——) follows primarily due to the effect of EI_{lag} (Table 6).

Further, the tails at both extrema have not reached as asymptotic state; hence statistical convergence has not been achieved. It is noted that, in the extreme cases, $CBM_{max.}$ reaches 100 N · m. Despite the nonconvergence state, the PDF provides an acceptable framework for the interpretation of modeled data trends.

The probabilities of the established $CBM_{max.}$ loads are analyzed in Fig. 15b using a CDF. The following probabilities of interest are extracted:

1) probability $CBM_{max.} \leq 34.50$ N · m (deterministic) is ≈16%,

2) probability that $CBM_{max.}$ exceeds an assumed critical load threshold of 75.00 N · m is ≈3% (Fig. 15b; Pr. [$CBM_{max.} \leq 75.00 \approx 0.97$; 1–Pr. ≈0.03),

3) probability that $CBM_{max.}$ is between the deterministic measure of 34.50 N · m and maximum assumed load threshold of 75.00 N · m is Pr. ($34.50 < CBM_{max.} < 75.00$) ≈ 82%, and critically

4) the 95% probability intervals translate to $CBM_{max.}$ domain of 32.00–65.40 N · m

The data presented in Fig. 15 quantify the loads distribution and the resulting probabilities due to stiffness uncertainties. In the case where extreme loads are evident, this information can be used as an aid for planform design modifications to ensure that structural failure due to excessive CBM loads is not realized.

C. Numerical Uncertainty and Sensitivity Analysis Versus Experimental Results

In this section, the uncertainties of the system are compared with experimental measurements at specific spanwise locations. The random outputs considered include both rotor power and blade structural loads. The surrogate-based approach presented in Sec. I is used to efficiently approximate rotor performance including structural loads at the 15 radial stations.

The analysis is structured to first consider the independent uncertainties in GJ, EI_{flap}, and EI_{lag}, and then the combined effects of the three parameters are modeled using a normal distribution, $\mathcal{N}(1.0, 0.20)$, centered about the mean with a standard deviation of 20%. In the proceeding section, statistical convergence for the quantification of uncertainty in rotor power is presented. Uncertainties in blade structural loads at defined radial stations are also detailed. SA is then undertaken to identify the impact of parameter uncertainties on response outputs.

1. Uncertainty Analysis for Rotor Power Using a Response Surface Model

A critical requirement in the generation of a response surface model (RSM) is to ensure that the approximation errors are low relative to target observations. When using the PCE method, the polynomial degree can significantly impact errors. To assess the accuracy of the system, the cumulative error of the outputs is formed and projected as a function of variance in database dimension and polynomial degree. Figures 16a and 16b summarize the cumulative

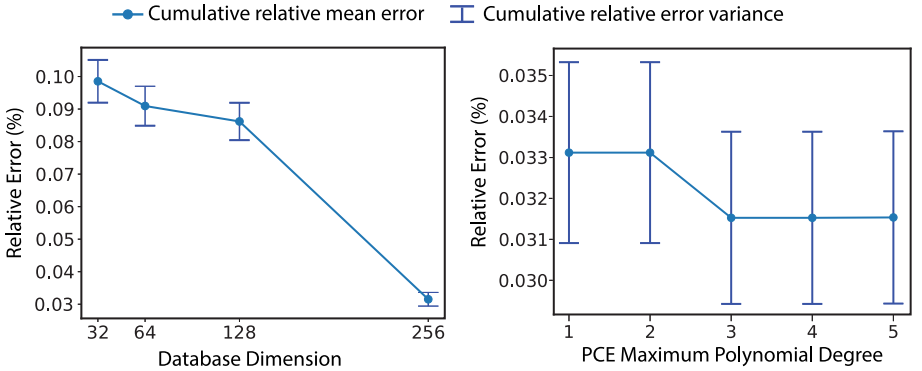

a) Database dimension dependency (3rd PCE order) **b) PCE maximum polynomial degree dependency (256 samples database)**

Fig. 16 PCE regression cumulative relative error evolution.

relative errors of all the uncertain outputs, where the former chart relates to the sampling of the input dimensions, and the latter focuses on the polynomial degree variation for a given input sampling dimension. The analysis confirms that with a sample size of 256 points using a polynomial degree of 3 (Fig. 16b), acceptable accuracy is achieved with an error of 0.031%. It is also noted that, even with 32 samples (Fig. 16a), the cumulative error is low and that it drops significantly with 256 sampling points. For the latter, the error is insensitive to a polynomial of degree greater than 3, as the random space is already well described by the calculated random outputs at the sampled locations.

An advantage of using an RSM is that statistical convergence can be established using an exhaustive MC approach with negligible computational effort as shown in Figs 17a–17d, where the population of input samples is increased from 10 to 50,000 points. At each incremental change, the statistical mean of total power (P_{tot}) and the 95% confidence interval (95% CI) are formed. The charts show that, when 50,000 evaluations are reached, both statistical metrics are converged for all uncertainty cases (single- and multidimensional uncertain variables problems). The corresponding PDF and CDF responses are also generated in Figs. 18 and 19, respectively, and it is confirmed that both curves have reached a stabilized shape. The best-fit PDF is a gamma law that is asymmetric and matches the response established using the global approach (Fig. 12). Table 7 summarizes the statistical convergence metrics for all uncertain cases. The confidence interval is negligible and the error factor is lower than 10^{-3}, hence confirming acceptable convergence.

Table 8 summarizes the total power uncertainty for the considered UQ cases. The PCE-established mean, the converged variance, and the 95% probability intervals are presented. The trends established are comparable with the results from the RCAS-based MCS in Table 3. It is shown that the isolated uncertainty that has the most influence is torsion stiffness, followed by flap stiffness, and lag stiffness uncertainty has a negligible impact. When the combined uncertainties are modeled, the variability around the mean matches the uncertainty in torsion stiffness alone. In Table 3, the width of the 95% probability interval for the combined effects was less than the interval width for the GJ effect alone (3.94 vs 4.13, respectively). This would confirm that the results in the Monte Carlo approach are not statistically converged with 1500 points, as the results with 50,000 samples using PCE (Table 8) confirm that the uncertainty widths for GJ and combined effects are in agreement. In follow-up works, a surrogate-based approach with RCAS simulations will also follow so that an extended input sampling size can be executed to sustain statistical convergence and to further validate this result.

2. *RSM-Based Blade Structural Loads Uncertainty Analysis*

Uncertainties are similarly quantified for the structural loads at set radial stations. Figures 20a–20c represent the comparison of the statistical mean and the resulting 95% probability interval with experimental data and the deterministic solution. It is observed that the experimental data are within the uncertainty range with exception to four measurements (2 for CBM in Fig. 20a; 1 for FBM in Fig. 20b; and 1 for TM in Fig. 20c) that are offset to the formed intervals. Also the 95% probability interval in some cases reaches 30% of the statistical mean, which is excessive and indicates a high sensitivity of the output at the respective radial station to the corresponding input parameter. The variability in the uncertain outputs is dependent on the characterization of the input uncertainties, and if a different input PDF were to be used, the resulting variability in the data relative to experiment and baseline will change accordingly.

The impact of combined uncertainties on the three moments is established in Figs. 21a–21c. Compared to the isolated uncertainties, the 95% probability intervals, in general, are wider for all cases, and results remain where the experimental data are not within the established uncertainty intervals. This can also be attributed to the setting and validation of the dynamic inflow model that was formed in Sec. II.B. The results also confirm that there are coupling effects in the responses due to the combined input uncertainties, and SA in the proceeding section will quantify these effects.

3. *Sensitivity Analysis Using the PCE Approach*

SA is a critical component in this workflow and can be integrated at UQ preprocessing or postprocessing stages. At preprocessing, SA is used to downselect to fewer variables that actively impact response output if the input dimensionality is extreme. At UQ postprocessing, SA is undertaken to study the level of contribution of each parameter

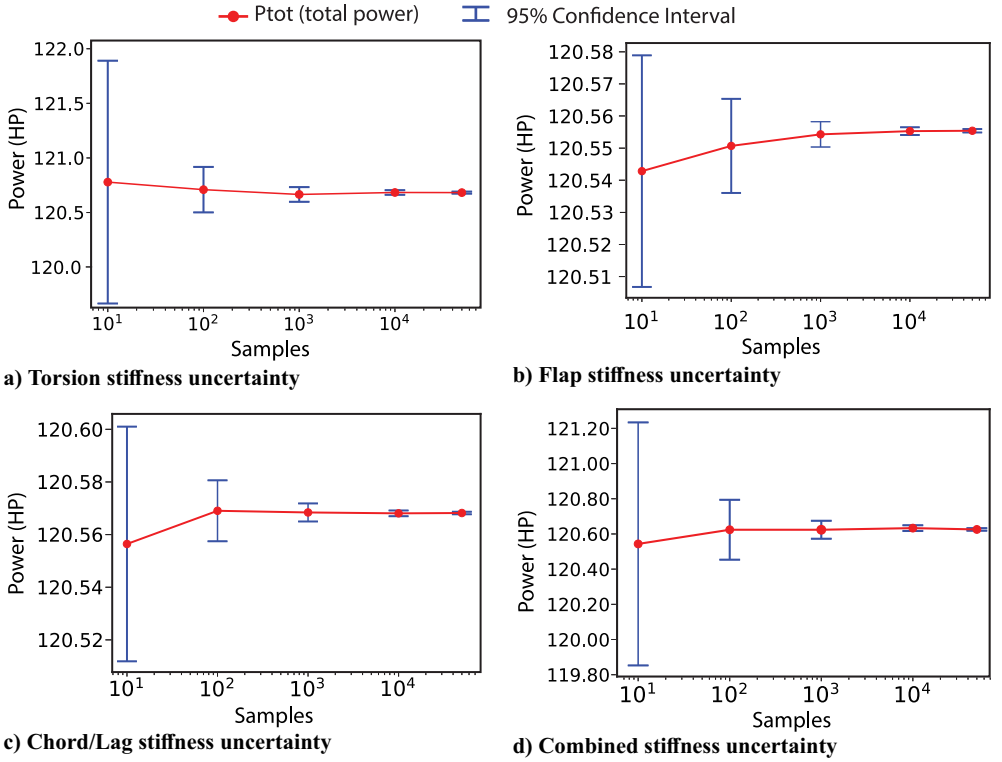

Fig. 17 Total power statistical mean convergence graphs for the four UQ problems.

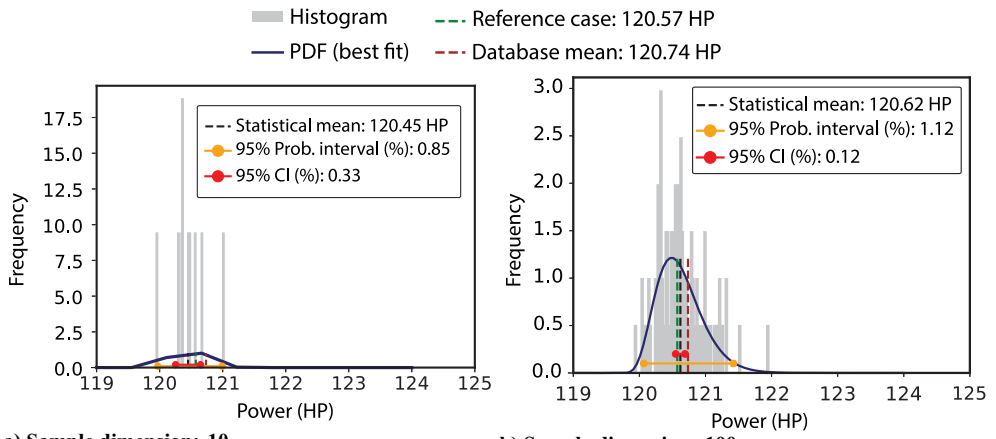

a) Sample dimension: 10

b) Sample dimension: 100

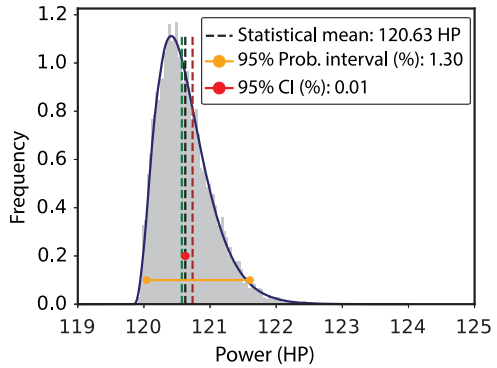

c) Sample dimension: 10,000

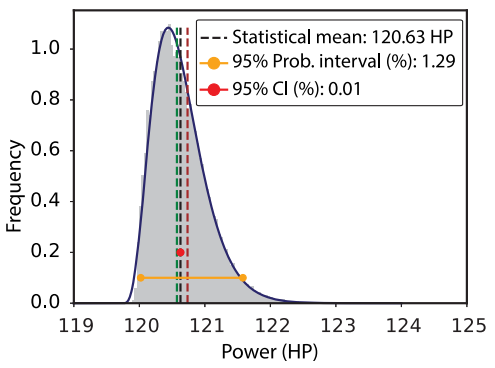

d) Sample dimension: 50,000

Fig. 18 Total power PDF convergence.

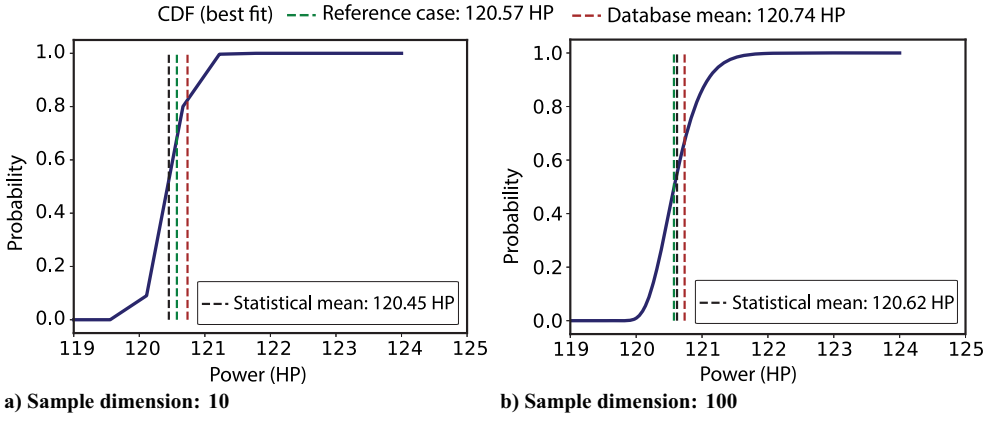

a) Sample dimension: 10

b) Sample dimension: 100

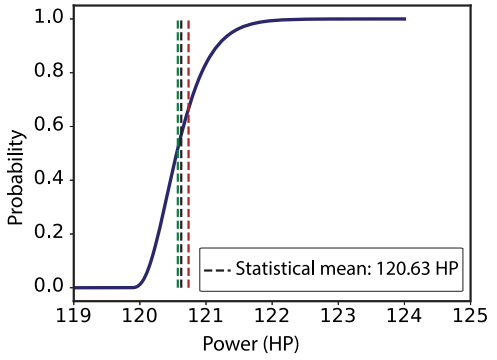

c) Sample dimension: 10,000

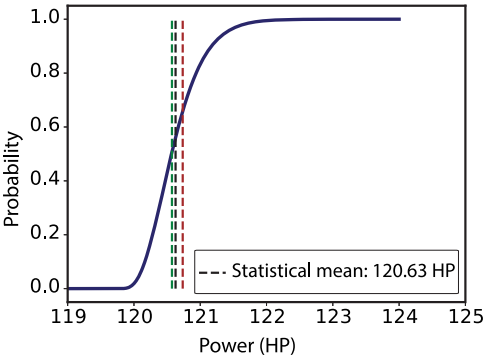

d) Sample dimension: 50,000

Fig. 19 Total power CDF convergence.

Table 7 Representation of normally distributed, $\mathcal{N}(1.0, 0.20)$, blade stiffness uncertainties on rotor power statistical mean value for converged 95% confidence interval

Uncertain stiffness	P_{req} (Det = 120.57 WP)	μ	σ	$Z_{a/2}\frac{\sigma}{\sqrt{n}}$	95% CI
GJ		120.69	0.52	0.00	(+120.68 to +120.69)
EI_{flap}		120.55	0.14	0.00	(+120.55 to +120.55)
EI_{lag}		120.56	0.03	0.00	(+120.56 to +120.56)
GJ, EI_{flap}, EI_{lag}		120.66	0.51	0.00	(+120.66 to +120.67)

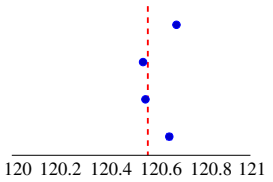

Table 8 Representation of normally distributed, $\mathcal{N}(1.0, 0.20)$, blade stiffness uncertainties on rotor power with 95% probability intervals

Uncertain stiffness	P_{req} (baseline = 120.57 HP)	μ	σ	95% Prob. interval
GJ		120.69	0.52	(+119.95 to +121.98)
EI_{flap}		120.55	0.14	(+120.40 to +120.95)
EI_{lag}		120.56	0.03	(+120.50 to +120.63)
GJ, EI_{flap}, EI_{lag}		120.66	0.51	(+119.92 to +121.90)

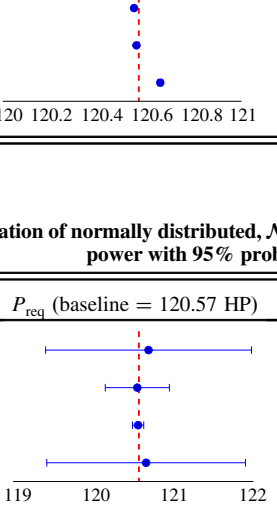

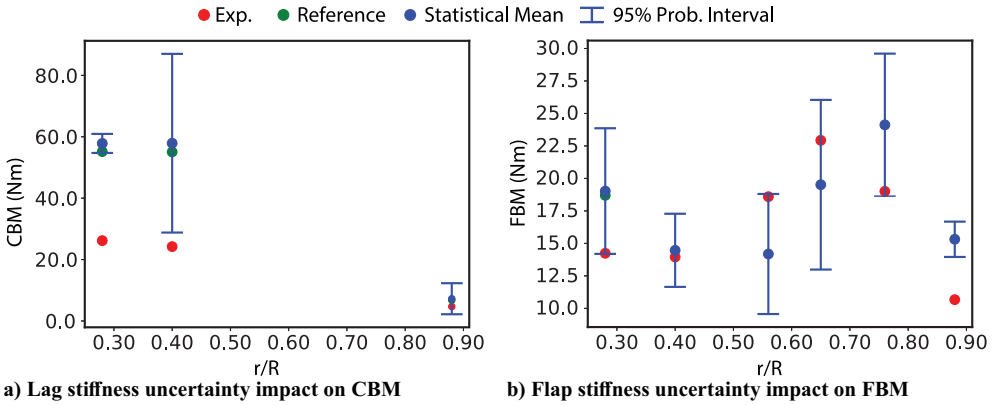

a) Lag stiffness uncertainty impact on CBM

b) Flap stiffness uncertainty impact on FBM

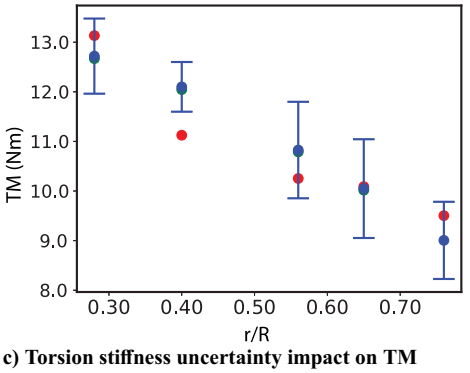

c) Torsion stiffness uncertainty impact on TM

Fig. 20 Impact of isolated stiffness uncertain on the corresponding moment.

on response outputs through independent perturbations and through interactions with other parameters. The knowledge gained from this process can be used to perform targeted studies in an effort to reduce the overall uncertainty of the system by focusing on parameter/s that are quantified with active influences on system response. In this work, SA is performed post-UQ for this purpose.

The PCE coefficients (Sec. III.B) that were previously established for the uncertainty analysis in Sec. IV.C are used to now compute the SIs. Figures 22a–22d summarize the calculated SIs (total and partial) and the corresponding nomenclature is defined in Table 9. In Fig. 22a, it is shown that total power is exclusively sensitive to torsion stiffness.

Parameter sensitivities on structural loads are presented in Figs. 22b–22d. For each moment modeled in the analyses, the sensitivity trends match irrespective of the spanwise location. As example, in Fig. 22b high total sensitivity of lag stiffness on TM (S2_tot) is noted at each radial station in comparison to the sensitivity attributed by torsion stiffness (S3_tot) that is relatively lower, and negligible sensitivity of flap stiffness (S1_tot) at the corresponding

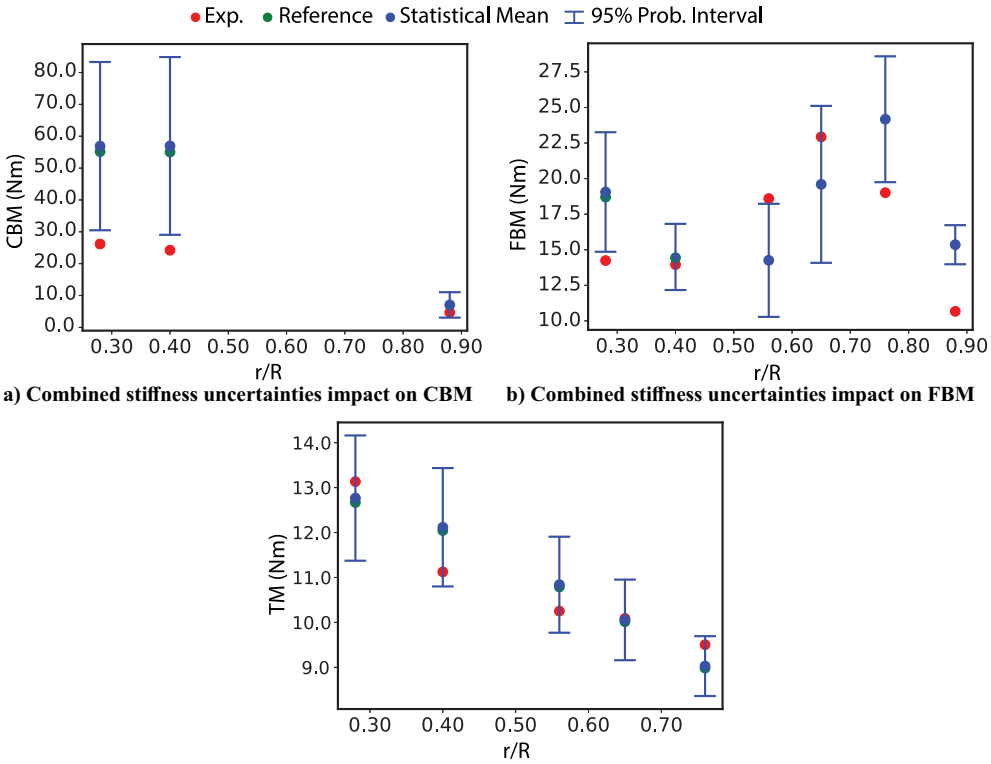

a) Combined stiffness uncertainties impact on CBM

b) Combined stiffness uncertainties impact on FBM

c) Combined stiffness uncertainties impact on TM

Fig. 21 Impact of Combined stiffness uncertainties on the three structural loads.

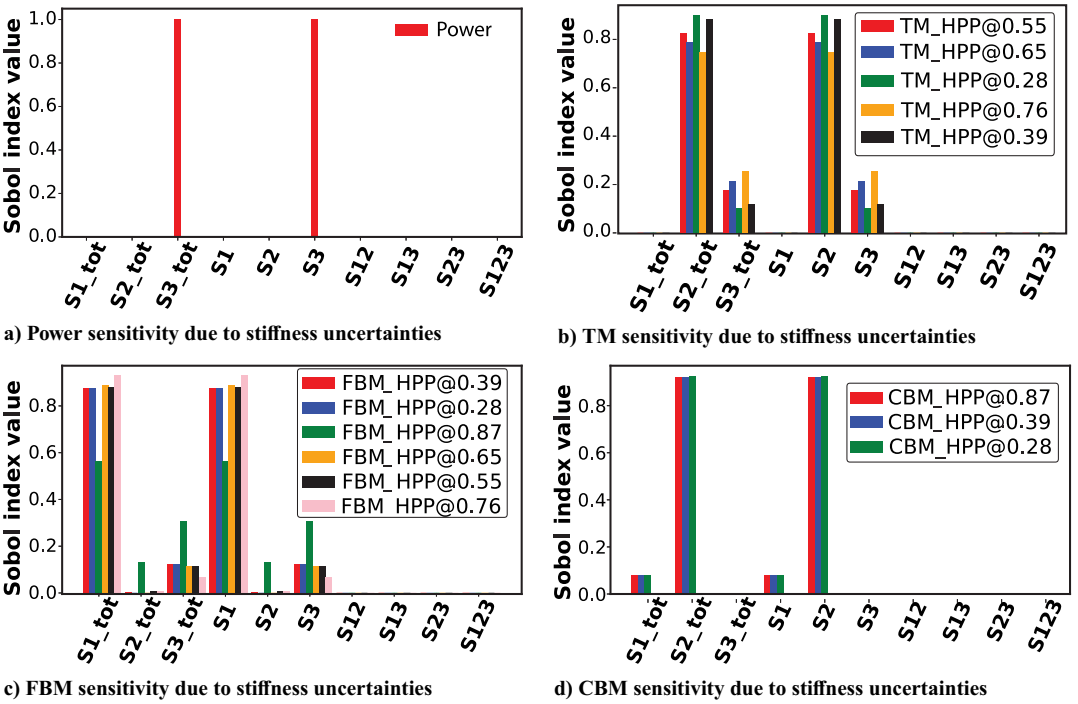

a) Power sensitivity due to stiffness uncertainties

b) TM sensitivity due to stiffness uncertainties

c) FBM sensitivity due to stiffness uncertainties

d) CBM sensitivity due to stiffness uncertainties

Fig. 22 Sensitivity plots for required power and moments under coupled uncertainties.

Table 9 Sobol indices correspondence table

Sobol index	Correspondence
_tot	Total value
1	EI_{flap}
2	EI_{lag}
3	GJ
12/13/23	2nd-order index
123	3rd-order index

span stations is noted. The result is further projected in Fig. 23a, where the 95% probability interval of TM due to uncertainty in lag stiffness is presented. The data confirm an extended uncertainty range across the span, hence validating the active sensitivity of lag stiffness on TM.

Similarly parameter sensitivities on FBM are presented in Fig. 22c. It is shown that flap stiffness (S1_tot) has high sensitivity to FBM, followed by torsion stiffness (S3_tot), and lag stiffness (S2_tot) that has a relatively muted impact with exception to span station $r/R = 0.87$. The distribution of spanwise FBM 95% probability

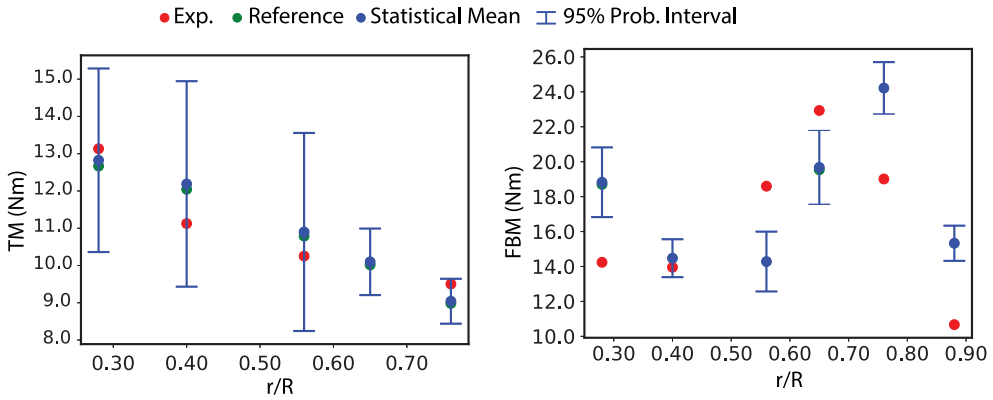

a) TM uncertainty range due to lag stiffness uncertainty

b) FBM uncertainty range due to torsion stiffness uncertainty

Fig. 23 Cross uncertainty ranges for TM and FBM.

intervals due to uncertainty in torsion stiffness is presented in Fig. 23b. The data show that the overall magnitude of uncertainty is generally consistent across the span, and close to the tip the intervals are reduced primarily since the blade is relatively stiff at this region due to the enforcement of the zero moment boundary condition.

The sensitivities of stiffness parameters on CBM at the modeled span stations are presented in Fig. 22d. It is shown that lag stiffness is actively influencing overall uncertainty with limited contribution by flap and negligible by torsion stiffness. Finally, no significant second- or third-order cross sensitivities are observed.

The results established using both uncertainty and SA facilitate the execution of intelligent, data-driven decisions. Uncertainty analysis quantified the magnitude of output variations from numerical predictions. Accordingly loads and performance envelopes were generated, which may deviate from target requirement. Supporting this effort were data derived from SA, which can be used as an information tool for targeted studies to follow in an effort to reduce the overall uncertainty of the system by focusing on input parameters that are identified as influential.

V. Conclusions

Uncertainty analysis is performed on the ONERA 7A rotor operating at high-speed condition to quantify the variability in blade stiffness properties (torsion stiffness GJ, flap stiffness EI_{flap}, and lag stiffness EI_{lag}) on rotor power and structural loads. Rotorcraft CA tools, including RCAS from the U.S. Army and HOST from ONERA, were used in the analysis. A validated structural and aerodynamic model was established for both RCAS and HOST. Uncertainty propagation then followed using MCS coupled with RCAS and a surrogate-based PCE method with HOST. The RCAS and HOST analyses showed that uncertainty in GJ was the influencing factor on overall uncertainty in rotor power relative to EI_{flap} and EI_{lag}. Additional analysis was also undertaken to quantify the uncertainty in maximum half peak-to-peak structural loads using RCAS. The largest uncertainty quantified was with peak CBM, where the overall uncertainty width exceeded ≈97% of the baseline deterministic analysis result. The data derived from HOST were further evaluated against measured half peak-to-peak structural loads across the blade span. A surrogate was then generated to approximate loads at each span station for the quantification of system uncertainties and sensitivities. It was shown that uncertainties in the blade stiffness significantly influence local structural loads. It was also observed that the experimental data were within the uncertainty range (95% probability interval) with exception of a few spanwise locations. A Sobol based analysis further demonstrated the benefits of performing SA to obtain a quantifiable measure of the level-of-impact of each blade stiffness parameter on rotor power and structural loads uncertainty. The computational efficiency demonstrated by a surrogate-based approach confirmed the benefits of integrating an RSM for rotorcraft aeromechanics uncertainty and SA.

As part of ongoing work efforts, the methodologies presented in this work will be used to address uncertainties with increasing complexity through the introduction of additional uncertain parameters. Higher-fidelity tools will be implemented and a combination of epistemic with aleatory uncertain parameters will be considered. As the number of uncertain inputs increases, it will be mandatory to identify and manage the respective dependencies on outputs. A critical requirement is to obtain a realistic representation of the uncertainty of the input aleatory parameters using a PDF. The uncertain outputs generated will then represent real-life uncertainty envelope, which can then be postprocessed with confidence to aid informed data-driven decision making.

Acknowledgments

This work is a result of a multiyear collaborative research under the U.S./French Partnership Agreement for Rotary Wing Aeromechanics and Human Factors Integration Research. The partners involve the U.S. Army DEVCOM AvMC Technology Development Directorate (TDD) and ONERA (The French Aerospace Lab).

References

[1] Wissink, A., Staruk, W., Tran, S., Roget, B., Lakshminarayan, V., Sitaraman, J., and Jayaraman, B., "Overview of New Capabilities in Helios Version 9.0," *57th AIAA SciTech Forum*, AIAA Paper 2019-0839, 2019.

[2] Cambier, L., Heib, S., and Plot, S., "The ONERA elsA CFD Software: Input from Research and Feedback from Industry," *Mechanics and Industry*, Vol. 14, No. 3, 2013, pp. 159–174. https://doi.org/10.1051/meca/2013056

[3] Siva, C., Murugan, M. S., and Ganguli, R., "Uncertainty Quantification in Helicopter Performance Using Monte Carlo Simulations," *Journal of Aircraft*, Vol. 48, No. 5, 2011, pp. 1503–1511. https://doi.org/10.2514/1.C000288

[4] Saberi, H., Hasbun, M., Hong, J. Y., Yeo, H., and Ormiston, R. A., "Overview of RCAS Capabilities, Validations, and Rotorcraft Applications," *American Helicopter Society 71st Annual Forum*, American Helicopter Soc., Alexandria, VA, May 2015.

[5] Dequin, A. M., Benoit, B., Kampa, K., von Grünhagen, W., Basset, P. M., and Gimonet, B., "HOST, A General Helicopter Simulation Tool for Germany and France," *56th Annual Forum of the American Helicopter Society*, American Helicopter Soc., Alexandria,VA, May 2000.

[6] Ortun, B., Potsdam, M., Yeo, H., and Truong, K., "Rotor Loads Prediction on the ONERA 7A Rotor Using Loose Fluid/Structure Coupling," *Journal of the American Helicopter Society*, Vol. 62, No. 3, 2017, Paper 032005. https://doi.org/10.4050/JAHS.62.032005

[7] Baurle, R., and Axdahl, E., "Uncertainty Quantification of CFD Data Generated for a Model Scramjet Isolator Flowfield," NASA Langley Research Center NF1676L-27196, Jan. 2018.

[8] Beran, P., Stanford, B., and Schrock, C., "Uncertainty Quantification in Aeroelasticity," *Annual Review of Fluid Mechanics*, Vol. 49, No. 1, 2017, pp. 361–386. https://doi.org/10.1146/annurev-fluid-122414-034441

[9] Stanford, B., and Massey, S., "Uncertainty Quantification of the FUN3D-Predicted Flutter Boundary on the NASA CRM," *58th AIAA/ASCE/AHS/ASC Structures, Structural Dynamics, and Materials Conference*, AIAA Paper 2017-1816, 2017.

[10] Lee, H., Ghia, U., Bayyuk, S., Oberkampf, W., Christopher, J., Benek, J., Rumsey, C., Powers, J., Bush, R., and Mani, M., "Development and Use of Engineering Standards for Computational Fluid Dynamics for Complex Aerospace Systems," *46th AIAA Fluid Dynamics Conference*, AIAA Paper 2016-3811, 2016.

[11] Singh, R., Corle, E., Jain, R., and Lim, J., "Computation and Quantification of Uncertainty in Predictions of HVAB Rotor Performance in Hover," *AIAA Scitech 2019 Forum*, AIAA Paper 2019-0285, 2019.

[12] Anusonti-Inthra, P., Corle, E., Smith, B., and Nieto, Z., "Sensitivity Analysis and Uncertainty Quantification of a Coaxial Rotor System," *AIAA Aviation 2019 Forum*, AIAA Paper 2019-3476, 2019.

[13] Murugan, S., Chowdhury, R., Adhikari, S., and Friswell, M., "Helicopter Aeroelastic Analysis with Spatially Uncertain Rotor Blade Properties," *Aerospace Science and Technology*, Vol. 16, No. 1, 2012, pp. 29–39. https://doi.org/10.1016/j.ast.2011.02.004

[14] Beaumier, P., Costes, M., Rodrigues, B., Polnot, M., and Cantaloube, B., "Weak and Strong Coupling Between the elsA CFD Solver and the Host Helicopter Comprehensive Analysis," *31st European Rotorcraft Forum*, Associazione Italiana di Aerotecnica e Astronautica (AIDAA), Florence, Italy, Sep. 2005, Paper 106.

[15] Yeo, H., Potsdam, M., Ortun, B., and Truong, K., "High-Fidelity Structural Loads Analysis of the ONERA 7A Rotor," *Journal of Aircraft*, Vol. 54, No. 5, 2017, pp. 1825–1839. https://doi.org/10.2514/1.C034286

[16] Pahlke, K., and Berend, G., "Chimera Simulations of Multibladed Rotors in High-Speed Forward Flight with Weak Fluid-Structure-Coupling," *Aerospace Science and Technology*, Vol. 9, No. 5, 2005, pp. 379–389. https://doi.org/10.1016/j.ast.2005.03.003

[17] Jain, R., and Yeo, H., "Effects of Torsion Frequencies on Rotor Performance and Structural Loads with Trailing Edge Flap," *Smart Material Structures*, Vol. 21, No. 8, 2012, Paper 085026. https://doi.org/10.1088/0964-1726/21/8/085026

[18] McKay, M., Beckman, R., and Conover, W., "Comparison of Three Methods for Selecting Values of Input Variables in the Analysis of Output from a Computer Code," *Technometrics*, Vol. 21, No. 2, 1979, pp. 239–245. https://doi.org/10.1080/00401706.1979.10489755

[19] Gamannossi, A., Amerini, A., Poggiali, M., Elmi, C., Mazzei, L., and Andreini, A., "Uncertainty Quantification of an Aeronautical Combustor Using a 1-D Approach," *AIP Conference Proceedings*, Vol. 2191, No. 1, 2019, Paper 020083. https://doi.org/10.1063/1.5138816

[20] Schaefer, J., Hosder, S., West, T., Rumsey, C., Carlson, J.-R., and Kleb, W., "Uncertainty Quantification of Turbulence Model Closure Coefficients for Transonic Wall-Bounded Flows," *AIAA Journal*, Vol. 55, No. 1, 2017, pp. 195–213.

[21] Dunn, M., Shotorban, B., and Frendi, A., "Uncertainty Quantification of Turbulence Model Coefficients via Latin Hypercude Sampling Method," *Journal of Fluids Engineering*, Vol. 133, No. 4, 2011, Paper 041402. https://doi.org/10.1115/FEDSM-ICNMM2010-30572

[22] García-Alfonso, H., and Córdova-Esparza, D., "Comparison of Uncertainty Analysis of the Monte Carlo and Latin Hypercube Algorithms in a Camera Calibration Model," *2018 IEEE 2nd Colombian Conference on Robotics and Automation (CCRA)*, Barranquilla, Colombia, 2018, pp. 1–5. https://doi.org/10.1109/CCRA.2018.8588138

[23] Hu, X., Chen, X., Parks, G., and Yao, W., "Review of Improved Monte Carlo Methods in Uncertainty-Based Design Optimization for Aerospace Vehicles," *Progress in Aerospace Sciences*, Vol. 86, Oct. 2016, pp. 20–27. https://doi.org/10.1016/j.paerosci.2016.07.004

[24] Scott, R., and Khurana, M., "Conceptual Design and Assessment of a Light Multirole Rotorcraft Using Uncertainty Quantification," *AIAA Scitech 2019 Forum*, AIAA Paper 2019-0558, 2019.

[25] Khurana, M., Russell, C., and Scott, R., "Uncertainty Quantification of a Rotorcraft Conceptual Sizing Toolsuite," *AIAA Scitech 2019 Forum*, AIAA Paper 2019-1728, 2019.

[26] Debusschere, B., Najm, P., Pebay, H. N., Knio, O., Ghanem, R., and Maitre, O., "Numerical Challenges in the use of Polynomial Chaos Representations for Stochastic Processes," *SIAM Journal on Scientific Computing*, Vol. 26, No. 2, 2004, pp. 698–719.

[27] Najm, H., "Uncertainty Quantification and Polynomial Chaos Techniques in Computational Fluid Dynamics," *Annual Review of Fluid Mechanics*, Vol. 41, 2008, pp. 35–52. https://doi.org/10.1146/annurev.fluid.010908.165248

[28] Hosder, S., Walters, R., and Perez, R., "A Non-Intrusive Polynomial Chaos Method for Uncertainty Propagation in CFD Simulations," *44th AIAA Aerospace Sciences Meeting and Exhibit*, AIAA Paper 2019-0891, 2006.

[29] Sudret, B., "Polynomial Chaos Expansions and Stochastic Finite Element Methods," *Risk and Reliability in Geotechnical Engineering*, edited by J. C. Kok-Kwang Phoon, CRC Press, Boca Raton, FL, 2015, pp. 265–300.

[30] Ghanem, R., and Spanos, S., *Stochastic Finite Elements: A Spectral Approach*, Springer, New York, 1991, https://link.springer.com/book/10.1007/978-1-4612-3094-6#bibliographic-information.

[31] Hastie, T., Taylor, J., Tibshirani, R., and Walther, G., "Forward Stagewise Regression and the Monotone Lasso," *Electronic Journal of Statistics*, Vol. 1, 2007, pp. 1–29. https://doi.org/10.1214/07-EJS004

[32] Sobol, I., "Sensitivity Estimates for Nonlinear Mathematical Models," *Mathematical Modelling and Computational Experiments*, Vol. 1, No. 4, 1993, pp. 407–414, https://www.scirp.org/(S(lz5mqp453edsnp55rrgjct55.))/reference/referencespapers.aspx?referenceid=2692473.

[33] Sobol, I., "Global Sensitivity Indices for Nonlinear Mathematical Models and Their Monte Carlo Estimates," *Mathematics and Computers in Simulation*, Vol. 55, No. 1, 2001, pp. 271–280. https://doi.org/10.1016/S0378-4754(00)00270-6

[34] Sudret, B., "Global Sensitivity Analysis Using Polynomial Chaos Expansions," *Reliability Engineering and System Safety*, Vol. 93, No. 7, 2008, pp. 964–979. https://doi.org/10.1016/j.ress.2007.04.002

[35] Rosenblatt, M., "Remarks on a Multivariate Transformation," *Annals of Mathematical Statistics*, Vol. 23, No. 3, 1952, pp. 470–472, http://www.jstor.org/stable/2236692.

[36] *Statistics and Machine Learning Toolbox™*, The MathWorks, Inc., Natick, MA, 2022, https://www.mathworks.com/products/statistics.html.

[37] Modeling, G., and Office, A., "Generalized Extreme Value Distribution and Calculation of Return Value," 2020, https://gmao.gsfc.nasa.gov/research/subseasonal/atlas/GEV-RV-html/GEV-RV-description.html [retrieved 14 Dec. 2022].

[38] Rieder, H., *Extreme Value Theory: A Primer*, Lamont-Doherty Earth Observatory, New York, Sept. 2014, https://www.ldeo.columbia.edu/~amfiore/eescG9910_f14_ppts/Rieder_EVTPrimer.pd.